UNIVERSITY OF TURKU

Development of a Semi-Autonomous System for High-Throughput Cyclic Voltammetry Measurements

Subject: Physics
Department: Department of Physics and Astronomy
Master's thesis

Author(s):
Xinyue Liu

23.6.2025
Turku

Master's thesis

Subject: Physics
Author(s): Xinyue Liu
Title: Development of a Semi-Autonomous System for High-Throughput Cyclic Voltammetry Measurements
Supervisor(s): Professor Pekka Peljo, Mousumi Dey, Dr. Sari Granroth
Number of pages: 64 pages
Date: 23.6.2025

Abstract

This thesis presents the development and validation of a semi-autonomous system designed to perform high-throughput cyclic voltammetry (CV) measurements, specifically tailored for the electrochemical characterization of iron-based redox complexes. Unlike existing systems primarily focused on either synthesis or electrode automation, this work innovatively integrates precision electrode positioning via a modified 3D printer with automated solution preparation using a pipetting robot, and a PalmSens4 potentiostat for reliable electrochemical data acquisition, addressing the reproducibility and efficiency limitations prevalent in manual and partially automated electrochemical systems.

Initial experiments validated the system's performance in preparing redox-active solutions, accurately positioning electrodes, and collecting CV data. Automation significantly reduced manual intervention, minimizing human-induced variability and improving the consistency and reproducibility of results. However, certain challenges emerged, notably the mechanical fragility of the pencil graphite electrodes used and the requirement for manual handling of CV scans, limiting complete automation.

To address the current limitations, future work will involve redesigning the well plate and employing 3D printing techniques by using carbon sheet at the bottom to serve as each well's working electrode. By doing this, previous pencil graphite electrodes' fragility issue and the labor-intensive process of physically replacing them will be avoided. Additionally, in order to improve communication between the potentiostat and 3D printer, a customized control core should be introduced to the system along with the needed PalmSens SDK. Each operation and measurement are carefully monitored. The system detects the electrodes' movement into and out of the well plate and responds in real time, under precise control. This modification is expected to make the system much more autonomous. Additionally, the experimental system will be set up in an atmosphere controlled by nitrogen or argon to reduce the interference brought on by dissolved oxygen. Such an inert atmosphere will broaden the scope of electrochemical research in a high throughput manner and make it easier to explore oxygen-sensitive metal complexes.

Overall, this semi-autonomous system represents a meaningful advancement toward fully automated electrochemical research workflows, offering substantial improvements in experimental throughput and data quality, thus accelerating the discovery of new electrochemical energy storage materials.

Key words: cyclic voltammetry, automation, electrochemical characterization, high-throughput screening.

Table of contents

1. Introduction

Automation in laboratory processes has increasingly become essential in scientific research, particularly in electrochemistry, where precision, reproducibility, and efficiency critically determine experimental success. Traditional manual methods, despite their utility, often suffer from inherent human-induced variability, limited throughput, and substantial time demands, particularly problematic in extensive experimental screenings and iterative optimization tasks. Recent advancements in robotics, artificial intelligence (AI), and machine learning (ML) have provided sophisticated tools to overcome these limitations, leading to the emergence of self-driving laboratories (SDLs). SDLs integrate robotic automation with intelligent algorithms, revolutionizing experimental workflows by autonomously managing tasks, optimizing reaction parameters, and systematically processing large datasets.[1,2]

To investigate if robotic solution handling and precise electrode positioning improve reproducibility and throughput in cyclic voltammetry measurements, this thesis develops a semi-automated measurement system integrating an automated liquid-handling robot, a modified consumer-grade 3D printer, and a PalmSens4 potentiostat.

This research demonstrates that automating crucial processes greatly enhances reproducibility, throughput, and operational efficiency, effectively overcoming limitations inherent to conventional manual techniques.

2. Background and Literature Review

2.1 Automation in Electrochemistry

A thorough literature overview of the important developments in automation-driven electrochemical research is presented in Chapter 2. It focuses especially on how predictive modeling and experimental parameter optimization brought about by machine learning (ML) have improved electrochemical analyses. Furthermore, robotics integration has significantly increased throughput, safety, and precision in electrochemical labs. The chapter also highlights the revolutionary potential of self-driving labs (SDLs), showing how advanced robotics and machine learning algorithms are facilitating autonomous experimentation and speeding up discoveries, particularly when it comes to high-throughput screening for new redox-active materials in energy storage applications.

2.1.1 Machine Learning in Electrochemistry

Machine learning algorithms have increasingly become vital tools in electrochemical research due to their ability to differentiate complex patterns from extensive datasets. Initial applications of ML in chemistry primarily involved predictive modeling, particularly for predicting chemical properties and behaviors. Originating in the mid-20th century from broader AI concepts, ML has gained substantial traction in chemical research and electrochemistry over the past two decades. This increase in application is largely due to the emergence of powerful computational resources, the accumulation of extensive datasets, and the need for more efficient and precise experimental methods.[3,4] Today, ML methodologies encompass broader functions, including high-throughput screening, reaction optimization, and the exploration of complex chemical spaces. This shift has significantly accelerated research processes traditionally reliant on labor-intensive and iterative experimental trials.[5,6]

Electrochemical research, inherently complex and data-rich, has notably benefited from the integration of ML techniques. To realize the full transformative potential of ML in

electrochemistry, certain foundational elements must first be established. Shkirskiy and Kanoufi (2024) list three needs for ML in electrochemistry: better data, automated experiments, and interdisciplinary experts. These challenges, inconsistent protocols, limited data access, and insufficient automation, are not unique to Single Entity Electrochemistry (SEE), a subfield focused on electrochemical responses at individual particles or molecular scales but apply broadly.[7] Their framework (Figure 1) essentially calls for standardizing methods and sharing data, which is something we also aimed for when designing our automated system. In practice, this means that our automation efforts must be coupled with careful data curation and method consistency to fully leverage ML, an approach we have tried to follow in this work. The provided schematic framework is thus generalizable for applying ML across various automated experimental platforms.

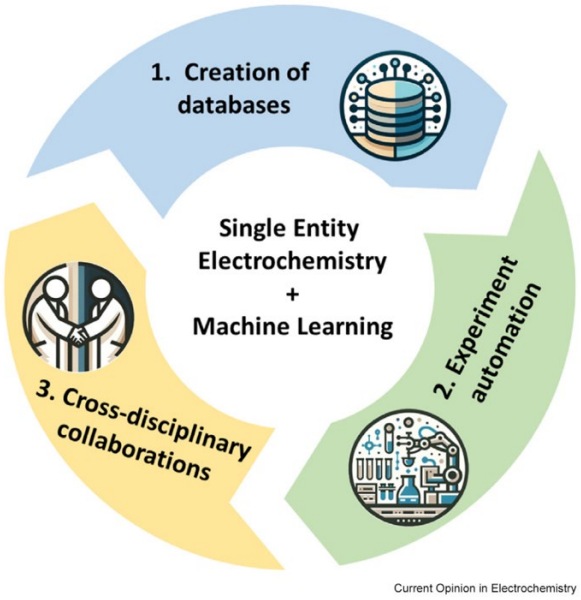

Figure 1. Schematic illustration of the essential requirements for the success of machine learning in the field of single entity electrochemistry. Reprinted with permission from Ref. [7]. Copyright 2024 Elsevier.

Furthermore, supervised ML models have successfully predicted critical electrochemical parameters, such as battery lifespans and electrode properties, thereby indicatively reducing traditional research and development timelines. For instance, Mistry et al. (2021) demonstrated how supervised ML methodologies could predict electrode mesostructure and porosity, effectively circumventing trial-and-error in

battery electrode design. In Figure 2 of their study, ML models (e.g. support vector machines) accurately forecasted how composition and processing conditions would affect the final porosity of lithium-ion battery cathodes.[5] Such examples underscore ML's power to replace or guide extensive experimental testing.

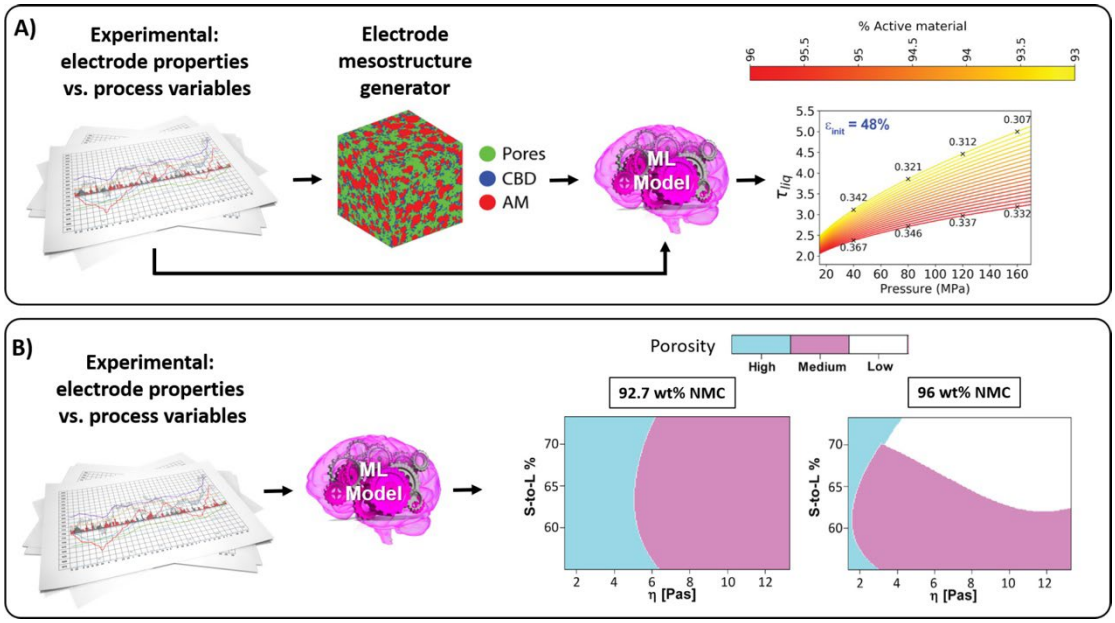

Figure 2. (a) Example of a workflow coupling experimental data, a surrogate electrode mesostructure predictor, and ML (Sure Independent Screening and Sparsifying Operator) to predict the impact of electrode composition, initial porosity, and calendered pressure on the electrode tortuosity factor. (b) Example of a classification machine learning algorithm (Support Vector Machine) able to predict the impact of the percentage of NMC active material, solid-to-liquid ratio, and viscosity of the slurry on the final porosity of a lithium-ion battery positive electrode. Reprinted with permission from Ref. [5]. Copyright 2021 American Chemical Society.

Additionally, advanced ML techniques like Bayesian inference and automated parameter inference have markedly improved the accuracy and efficiency of electrochemical analyses, particularly within quantitative voltammetry. Gundry et al. (2021) underscored the transformative impact of these methods: by efficiently handling large voltametric datasets, ML algorithms can elucidate complex electrochemical mechanisms and extract precise quantitative parameters that were previously challenging to obtain via conventional methods. Though their proposed framework was developed for Fourier-transformed alternating current voltammetry, its implications extend broadly. Their schematic flowchart (Figure 3) demonstrates

how ML-driven strategies, paired with intelligent parameterization routines, can streamline data interpretation by automatically classifying reaction mechanisms and determining kinetic parameters.[4] While the focus of this thesis is on experimental automation and cyclic voltammetry (CV) data acquisition, these advances highlight the importance of developing complementary data analysis workflows. In a forward-looking sense, such ML-based analytics align with the overarching goal of autonomous experimentation that is not only to automate measurements but also to accelerate interpretation and discovery.

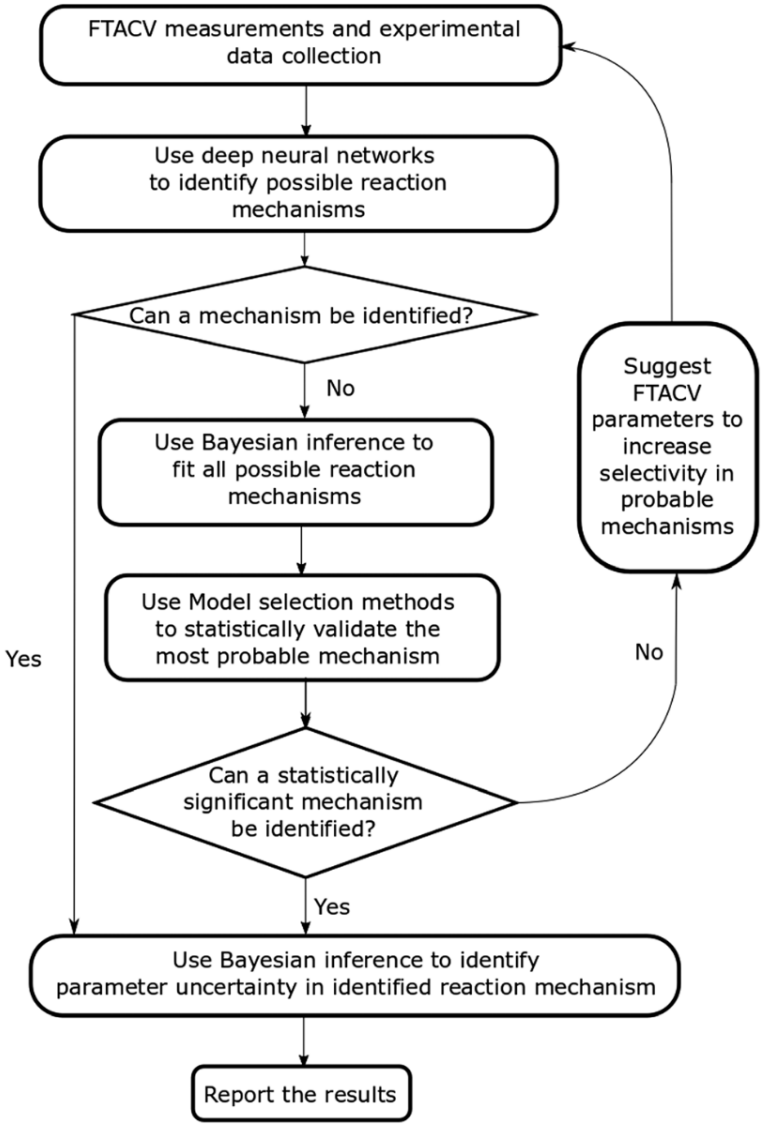

Figure 3. Proposed artificial intelligence flowchart for analysis of Fourier transformed alternating current (FTAC) voltammetric experimental data. Reprinted with permission from Ref. [4]. Copyright 2021 Royal Society of Chemistry.

In short, the importance and advantages of ML in chemical and electrochemical research are considerable. ML methodologies enable researchers to rapidly screen extensive chemical and experimental conditions, efficiently identify optimal scenarios, and greatly expedite the discovery and optimization process. The effectiveness of ML in electrochemistry, however, critically depends on high-quality, centralized databases and standardized experimental protocols. Establishing such infrastructure ensures the reproducibility and accuracy of data-driven predictions, ultimately enhancing research efficiency and reducing costs associated with manual experimentation. These data-centric advancements form a crucial backdrop for the automation efforts described in this thesis.

2.1.2 Robotics in Electrochemistry

Robotics integrates mechanical systems, sensors, and software to autonomously execute complex laboratory tasks. Since the late 20th century, robotics has transitioned from basic functions like reagent handling to sophisticated automated synthesis and electrochemical analysis.[8]

Erichsen et al. (2005) developed a robotic system for electrochemical measurements with specifically script language. Using stepmotor to ensure the position precision, they successfully performed complicated electrosynthesis in standard microtiter plates.[9] Another early innovations was the ORPHEUS-HOPE platform by Nejdl et al. (2015). They employed robotic arms fitted with electrochemical sensors for remote environmental analysis, demonstrating how automation can perform tasks in inaccessible conditions with high precision. As shown in Figure 4, this robotic platform utilized a combination of printed electrodes (carbon paste working electrode, Ag/AgCl reference electrode, and platinum auxiliary electrode) mounted on a robotic arm, enabling real-time analysis of environmental samples in hazardous conditions inaccessible to humans.[8] Such examples established that robotic systems could expand the reach of electrochemical techniques beyond traditional lab settings.

PARAMETER	VALUE
ROBOT DIMENSIONS	881x590x426mm
WHEEL DIAMETER	426mm
WEIGHT	42 kg
BATTERY OPERATION	90 mins to 4 hours
OPERATING TEMPERATURES	-32˚C to 85˚C
CHARGING VOLTAGE	18-32 V
MAX. CHARGING CURRENT	5A
MAX. SPEED	3.6km/h
MAX. OBSTACLE HEIGHT	20 cm
CLIMB ABILITY	31˚
MAX. REACH (CABLE)	100 m
MAX. REACH (WIRELESS)	1km (line-of-sight)

Figure 4. (A) Photography of robotic platform ORPHEUS-HOPE with operator, a = pan/tilt color camera, b = high resolution color camera, c = one degree of freedom manipulator with holder on screen printed electrodes, d = operator controlling the robot using visual telepresence. Reprinted with permission from Ref. [8]. Copyright 2015 Elsevier.

5Similarly, Haghighi et al. (2025) introduced an underwater "robo-sensor" with integrated electrodes for real-time monitoring, highlighting the reliability and stability gains from robotic control in electrochemical measurements (see Figure 5). Their submersible robotic sensor operated continuously, indicating how robotics can improve data collection in challenging conditions by maintaining consistent measurement protocols that would be difficult for humans to replicate underwater.[10]

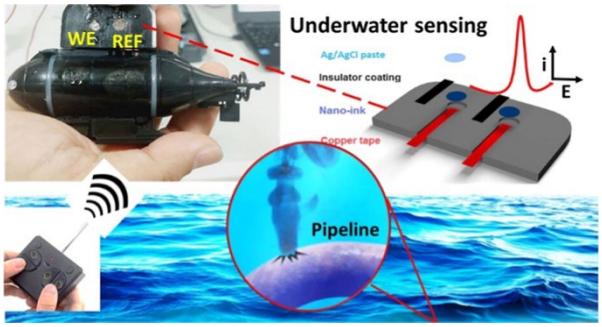

Figure 5. Innovative Electrochemical Nano-Robot. Reprinted with permission from Ref. [10]. Copyright 2025 American Chemical Society.

These applications underscored the advantages of robotics in terms of enhanced safety, extended operational range, and improved consistency in data quality.

6More recent efforts have integrated robotics with AI to create autonomous electrochemical discovery systems. A notable example is the ECARUS platform developed by Laws et al. (2024), a robotic system that autonomously performed

solution-phase synthesis and electrochemical characterization using probabilistic algorithms. Figure 6 shows the ECARUS platform, which could autonomously run thousands of CV experiments without human input. It would iteratively adjust parameters based on prior results, rapidly exploring the chemical parameter space. Through this learning cycle, ECARUS identified new redox-active complexes with improved performance.[11] This platform exemplifies how integrating robotics with AI can massively boost experimental throughput and reproducibility.

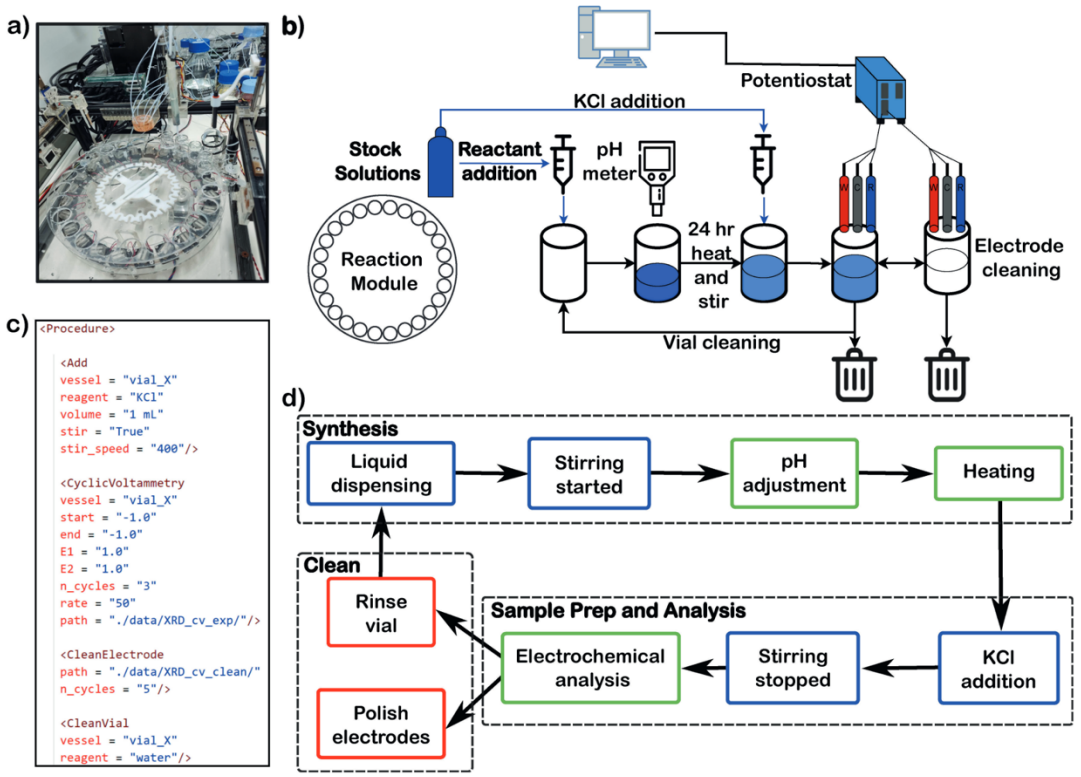

Figure 6. Components in the ECARUS self-driving platform. (a) Picture of the robotic platform (ECARUS), (b) Representation of the platform; highlighting the main components required for each step, (c) XDL procedure for running the electrochemical analysis (d) general synthetic protocol used by ECARUS, outlining the 3 main physical steps performed by the platform. Reprinted with permission from Ref. [11]. Copyright 2023 Chemical Europe.

Another crucial aspect of modern robotics is the software that controls these systems. High-level programming languages such as Python and MATLAB have become essential tools for developing control algorithms, simulation models, and instrument interfaces in laboratory robotics. For example, Chaos *et al.* (2013) demonstrated that a unified virtual/remote lab environment combining LabVIEW and MATLAB allowed researchers to develop and test robot control algorithms in simulation and then

seamlessly deploy them on real electrochemical robots[12]. More recently, there has been a broad trend toward open-source software in robotics: Kantaros *et al.* (2025) emphasize the growing adoption of languages like Python in both industry and academia as flexible alternatives to proprietary tools, due to their low cost and strong community support.[13] This integration of robust software control with electrochemical robotics underpins the reliable operation of our own automated pipetting robot and 3D printer systems, as described later in this thesis. In essence, sophisticated software, whether via established platforms like LabVIEW/MATLAB or open-source frameworks like Python, enables precise synchronization of robotic motions with electrochemical processes, ensuring experiments are executed consistently and safely.

Overall, robotics in electrochemical research provides numerous advantages, including improved reproducibility, reduced human-induced variability, enhanced safety (by minimizing exposure to hazardous substances), and significant acceleration of experimental throughput.

2.2 The role of Automation in Self-Driving Laboratories (SDLs)

From previous section, it has been proved that recent advancements in artificial intelligence (AI) and robotics have substantially altered traditional laboratory operations, ushering in the era of self-driving laboratories (SDLs) in the field of materials science and electrochemistry. As mentioned in the Introduction, self-driving laboratories (SDLs) combine automated robotics with intelligent algorithms to perform and optimize experiments autonomously. Here we expand on two specific pillars of SDL automation relevant to this thesis: **(i)** the use of automated pipetting robots for chemical solution handling, and **(ii)** the use of computer-aided design (CAD) and 3D printing to create custom lab hardware. In the following subsections, we examine each of these aspects and highlight literature examples that illustrate their roles, thereby contextualizing how they support the semi-autonomous system developed for high-throughput CV in this work.

2.2.1 Role of Pipetting Robots in Automated Chemistry

Automated liquid-handling robots, essentially “pipetting robots”, play a central role in many SDLs by preparing solutions and handling reagents with high precision and throughput. Replacing manual pipetting with robotic systems improves volumetric accuracy and reproducibility, while also enabling parallel processing of multiple samples. This capability is crucial in high-throughput chemistry, where dozens or hundreds of experiments (for example, preparing electrolyte solutions or combinatorial reaction mixtures) must be carried out under consistent conditions. By eliminating human pipetting errors and fatigue, robotic liquid handlers ensure that each experiment is conducted with nearly identical reagent volumes and mixing protocols, which is essential for reliable comparisons and data quality. It is for these reasons that many SDL implementations incorporate dedicated pipetting robots or automated dispensing modules to manage solution preparation steps.

Several prominent examples demonstrate the impact of pipetting robots in automated chemistry. ORGANA, a recently developed SDL platform by Darvish et al. (2025), showcases how AI-driven robots can execute complex experimental protocols that include solution handling. In ORGANA, a robotic system interprets high-level instructions (via natural language processing) and performs tasks such as reagent dispensing, mixing, and analytical measurements autonomously.[14] Figure 7 illustrates this versatility: ORGANA’s robot conducts diverse chemistry experiments, from solubility tests to recrystallizations and pH measurements, by carrying out the required liquid transfers and manipulations without human intervention. This parallel execution of multiple liquid-handling tasks majorly boosts experimental throughput and minimizes human error in chemical workflows.

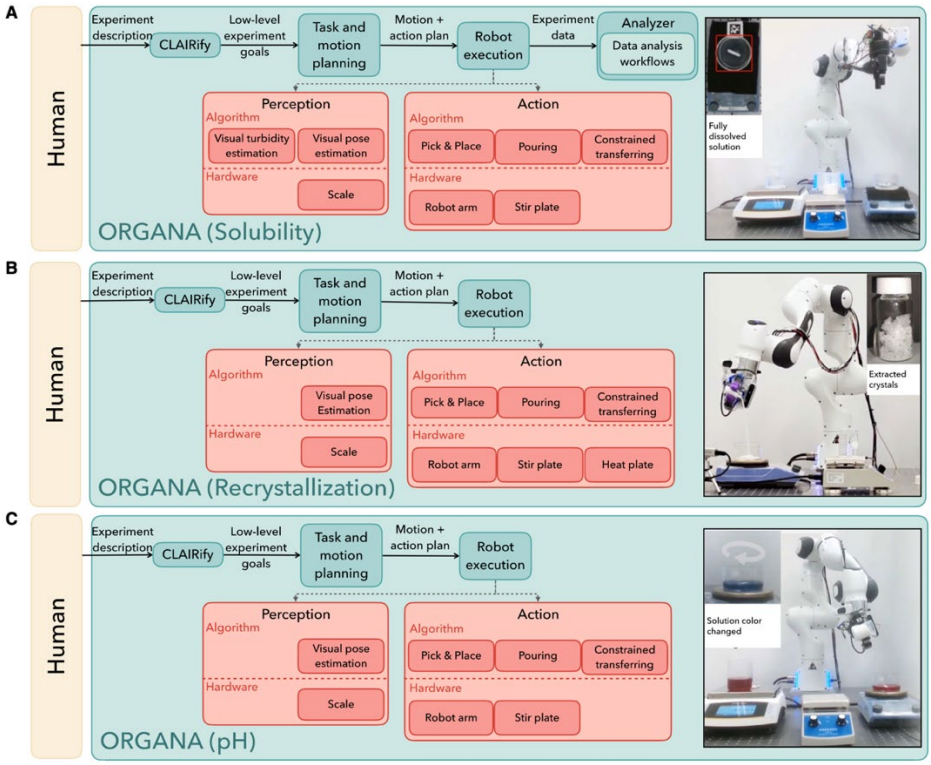

Figure 7. Instances of ORGANA conducting various chemistry experiments (A) Solubility, (B) recrystallization, and (C) pH testing. Snapshots depict the robot executing actions in each setup alongside images of the end results. Reprinted with permission from Ref. [14]. Copyright 2025 Elsevier.

7Another illustrative platform is the “Ada” self-driving laboratory developed by MacLeod et al. (2020) for materials chemistry. Ada is built on a modular robotic arm that can switch between tools to perform different functions. Notably, it features a pipetting system: the robot arm can pick up disposable pipette tips and dispense liquids with high accuracy, using an integrated syringe pump for precise volume control. Figure 8 shows the Ada platform equipped for thin-film synthesis, where module (B) highlights the fluid-handling setup, the robot’s pipette mount and tips, enabling automated solution transfer, while module (C) handles substrate manipulation. By automating both liquid dispensing and substrate processing, Ada accelerates experiment workflows (such as preparing precursor solutions and depositing them on substrates) with minimal user input[15]. This underscores how pipetting robots contribute to a broader SDL to ensure each batch of experiments (e.g. coating a series of films or preparing multiple samples) is prepared uniformly, which in turn improves the reliability of subsequent measurements (like film characterization

or electrochemical tests).

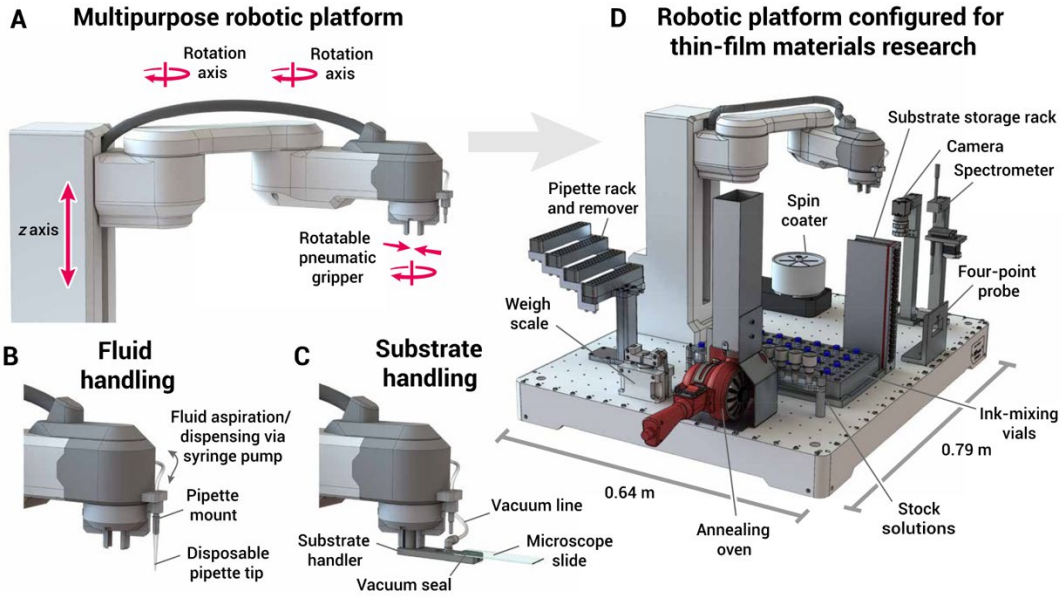

Figure 8. The Ada self-driving laboratory. Reprinted with permission from Ref. [15]. Copyright 2020 American Association for the Advancement of Science.

8In the field of high-throughput synthesis, the importance of automated liquid handling is further exemplified by a self-driving nanoparticle synthesis platform developed by Salley et al. (2020). This platform was designed to autonomously optimize the synthesis of gold nanoparticles (AuNPs) using a genetic algorithm. A bank of robotic liquid handlers, including multiple syringe pumps and a custom dispensing stage, is used to combine reagents in a series of small-scale reactions without human help. Figure 9 depicts the system's key components, such as the tri-syringe pump assembly for reagent delivery and a Geneva wheel mechanism that shuttles vials to various stations (mixing, analysis, etc.). The robotic platform sequentially dispenses controlled volumes of stock solutions into vials, mixes them, and then automatically measures each reaction's outcome (via in-line UV-Vis spectroscopy). By iterating through generations of experiments, dispensing new mixtures based on the genetic algorithm's suggestions, this system can efficiently navigate the chemical parameter space. Crucially, the automated pipetting and dosing ensure that each AuNP synthesis experiment is executed with consistent timing and volumes, so the feedback to the algorithm is based on truly comparable trials.[16] This closed-loop approach would be impractical without a reliable liquid-handling robot to

carry out dozens of reactions and measurements in a reproducible manner.

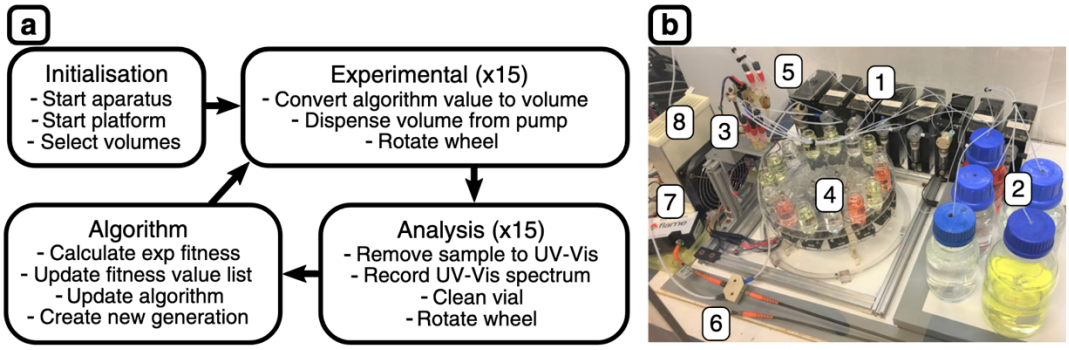

Figure 9. General operating outline and top view of the robot for the controlled synthesis of AuNPs. a Summary of the initialization of the platform, the experimental and analysis sequences and the algorithm operations for a single generation of reactions. b The platform consisting of (1) tri-continent C3000 syringe pumps, (2) reagent bottles on stirring plate, (3) dispensing stage, (4) geneva wheel with vial tray, (5) sample extraction module, (6) flow cell/optics, (7) ocean optics flame UV-Vis spectrometer and (8) heating element. Reprinted with permission from Ref. [16]. Copyright 2020 Springer Nature.

Beyond these large-scale platforms, even the adaptation of smaller-scale or low-cost pipetting robots has proven valuable. For example, Councill et al. (2021) modified a benchtop open-source pipetting robot (Opentrons OT-1) to accurately handle nanoliter volumes, vastly extending the robot's original capabilities. Their low-cost system was shown to reproducibly dispense as little as 50 nL with under 5% error, performance on par with commercial liquid handlers costing an order of magnitude more. Such work demonstrates that bespoke enhancements (in this case, installing a custom syringe and camera system) can adapt pipetting robots for specialized tasks, like preparing microvolume analytical samples, thereby broadening the scope of automated chemistry accessible to researchers on a budget.[17]

In summary, automated pipetting systems have become indispensable in chemical automation. They ensure high precision and consistency in solution preparation, free researchers from tedious manual work, and enable the execution of complex or high-throughput experimental plans that would otherwise be prohibitively time-consuming. In the context of this thesis, the Opentrons OT-2 robot serves exactly these purposes: it automates the preparation of redox-active solutions for CV measurements, guaranteeing that each sample is prepared with the same rigor and accuracy. This

consistency in sample preparation lays the foundation for fair comparisons in our high-throughput electrochemical experiments.

2.2.2 Role of Computer-Aided Design (CAD) and 3D Printing in SDLs

While intelligent software and robots execute experiments, custom-designed hardware is often needed to adapt these tools to specific laboratory tasks. In self-driving labs, researchers frequently face unique engineering challenges, such as holding a particular sensor in place, interfacing a robot arm with lab glassware, or arranging multiple reaction vessels for parallel processing. Computer-aided design (CAD) and 3D printing have emerged as powerful enabling technologies to meet these needs. CAD software allows rapid prototyping of customized parts, which can then be fabricated with 3D printers or other additive manufacturing techniques. The resulting custom components (e.g., specialized holders, adapters, reaction cell architectures) can seamlessly integrate with robotic platforms, extending their capabilities.[13,17–20] This approach essentially accelerates development cycles for SDL hardware: instead of waiting for costly custom-machined parts, researchers can design, print, and test a component within days. The flexibility of 3D printing also means designs can be quickly iterated and optimized. In the context of automated chemistry and electrochemistry, this has led to the creation of tailor-made devices such as printed electrode assemblies, liquid transfer modules, and robot tool mounts that are not available off-the-shelf.[3,16,17,21] By leveraging CAD and 3D printing, self-driving lab developers ensure that their automation platforms are equipped with hardware precisely suited to their experimental goals.

Examples from recent literature highlight the pivotal role of custom CAD-designed components in automation. Silva et al. (2021), for instance, demonstrated how extensive use of 3D printing can yield customized electrochemical cells and device housings. In their work, various 3D printing technologies were employed to fabricate tailored reaction wells and electrode holders (see Figure 10), showcasing additive manufacturing's rapid prototyping capability for electrochemical applications.[20] This

allowed the researchers to quickly iterate on cell designs for different experiments, something that would be difficult and time-consuming with conventional fabrication methods. It underlines a general trend in which SDLs rely on custom-fabricated hardware to achieve functionalities not possible with standard labware.

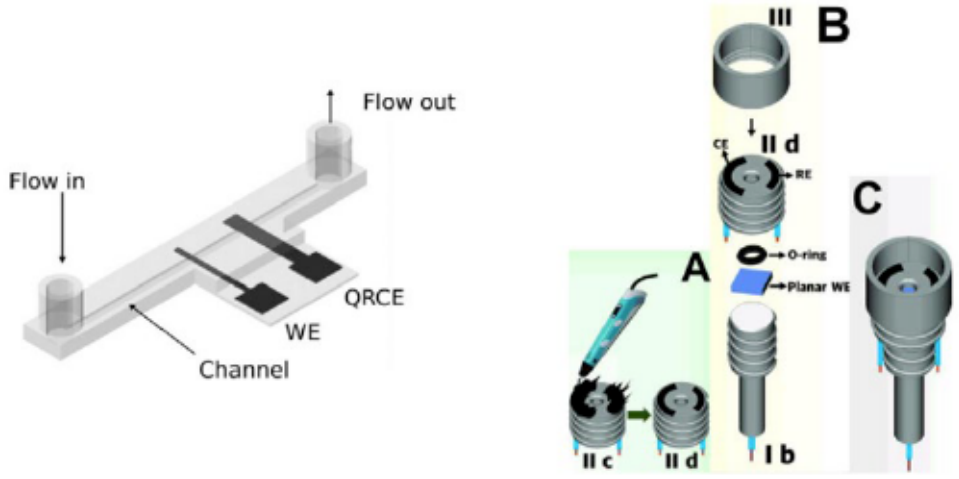

Figure 10. (left) 3D-printed graphene-PLA electrodes. Reprinted with permission from Ref. [22]. Copyright 2019 Elsevier. (right) 3D-printed carbon black-PLA counter and reference electrodes (II c and II d in A) using the 3D pen and planar working electrodes. Reprinted with permission from Ref. [19]. Copyright 2021 Elsevier.

In this thesis, the integration of CAD and 3D printing is central to the design of the semi-autonomous CV measurement system. A key challenge addressed by our work was how to precisely position electrodes into multiple small wells for sequential measurements. Rather than relying on existing lab equipment, we engineered a custom solution, a miniaturized three-electrode holder tailored to a 3D printer frame. Using CAD software, the electrode holder was designed to securely mount a working, reference, and counter electrode at fixed distances from each other, matching the dimensions of standard well plates. This digital design was then produced with a 3D printer, yielding a robust part that could attach to the z-axis of a Prusa 3D printer. By repurposing the Prusa 3D printer as an XYZ positioning robot and outfitting it with the 3D-printed electrode holder, our system achieves accurate and reproducible electrode placement in each well. The success of this approach underscores how CAD and additive manufacturing enable rapid customization of hardware for automation.

Within a short development cycle, we created a specialized tool that interfaces a standard 3D printer with electrochemical cells, something not available off-the-shelf. Moreover, the printed holder offers the flexibility to be re-designed and re-fined as needed (for instance, to accommodate different electrode sizes or well plate formats), exemplifying the adaptability of 3D-printed solutions.

By integrating CAD-designed 3D-printed components, our semi-autonomous platform addresses experimental needs that conventional equipment could not readily solve. In this case, maintaining consistent electrode geometry and alignment across high-throughput CV tests. This approach is in line with the broader SDL trend of using custom hardware to enhance automation capabilities. It also goes a step further: whereas prior platforms like those by Silva et al. (2021) focused on printing static devices, our work incorporates a 3D printed part into an active robotic system (the modified printer), marrying rapid prototyping with motion control. In summary, CAD and 3D printing are indispensable in self-driving labs for creating bespoke automation hardware, and in this thesis, they enabled the development of a unique electrode positioning system that is crucial for reliable, high-precision electrochemical measurements. Each figure and example discussed, from printed electrochemical cells[20] to custom robotic modules in Ada[15] and the geneva-wheel system for nanoparticle synthesis[16], reinforces the idea that the ability to design and fabricate tailor-made parts is often the limiting factor that transforms a collection of machines into a coherent, task-specific autonomous laboratory. Our system leverages this paradigm to bridge the gap between standard laboratory tools (pipettes, electrodes, etc.) and fully automated operation, illustrating how the fusion of pipetting robotics with CAD-engineered 3D-printed hardware can advance electrochemical research toward greater autonomy and throughput.

2.3 Automation and High-Throughput Screening in Redox Flow Battery Research

Redox Flow Batteries (RFBs) have become increasingly prominent for medium- to

large-scale energy storage applications, particularly due to their flexible energy capacity, modular design, scalability, rapid response, and the possibility of independent tuning of power and energy. Despite these substantial benefits, there are critical challenges that currently hinder their widespread commercial adoption, primarily related to cost, safety, and performance limitations.

One of the most extensively researched and deployed RFB technologies is the all-vanadium redox flow battery (VRFB), favored due to its avoidance of electrolyte cross-contamination and relatively stable electrochemical properties. However, the widespread application of VRFB technology faces notable drawbacks due to the high cost and limited availability of vanadium resources. Furthermore, the electrolyte solutions used in VRFBs, although more stable than other chemistries, pose safety risks and environmental concerns due to their acidity and the toxic nature of vanadium ions.[23]

These limitations underline a strong necessity for developing alternative, next-generation RFB chemistries with more abundant, safer, and cost-effective materials. Consequently, a substantial amount of research has been directed towards exploring various organic and non-toxic inorganic redox-active materials. Each of these new chemistries, however, requires careful optimization across multiple performance parameters, including redox potential, solubility, chemical stability, and kinetic properties, to ensure their viability as practical energy storage solutions.[24]

Traditional research methodologies in developing these next-generation battery materials have predominantly followed a trial-and-error approach, prominently constraining the pace of discovery and optimization. Such methods are time-consuming and resource-intensive, as they rely heavily on manual experimentation that limits the volume and consistency of data collected. This drawback has highlighted the necessity and utility of automated systems and high-throughput screening methods in battery research.

Automation and high-throughput experimentation have increasingly been adopted as

transformative methodologies to overcome these limitations by accelerating battery materials research, discovery, and optimization processes. Automated systems allow large-scale parallel experiments to be executed consistently and reproducibly, drastically improving the efficiency and quality of collected data. Liang et al. (2023) demonstrated the effectiveness of robotic platforms for high-throughput solubility measurements, which play a critical role in designing new electrolyte formulations for both aqueous and non-aqueous RFB systems. As shown in Figure 11, this work reported the successful development of an optimized negative electrolyte formulation, using automated high throughput platforms, that considerably improved the energy density and stability of a ferrocyanide-based redox flow battery. This battery demonstrated stable cycling performance over 18 days (>100 cycles), along with a substantial increase in energy density by 24%, underlining the impactful role of high throughput methods in practical battery improvements. It highlights the importance of standardized automated workflows in generating large-scale, high-quality datasets necessary for effective data-driven material discovery.[25] These approaches not only enhance the efficiency of research processes but also contribute to a deeper understanding of structure-property relationships, laying a robust foundation for future advancements in next-generation RFB chemistries.

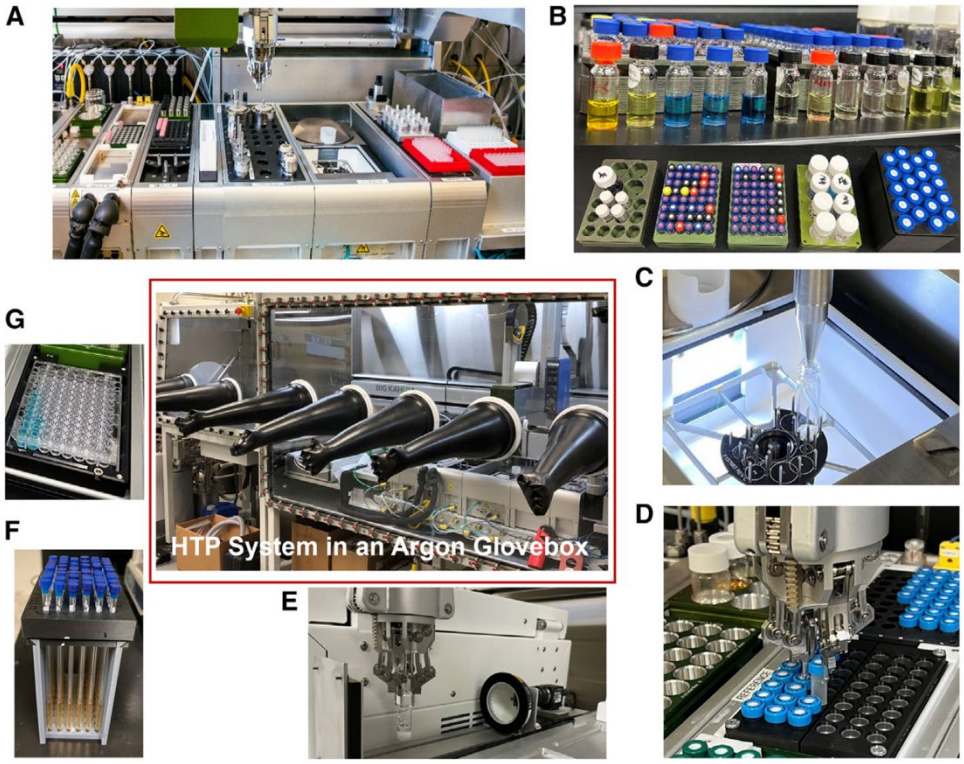

Figure 11. Photographs of a customized robotic platform (Big Kahuna, Unchained Labs) with key functions listed (A) Inside view of the platform. (B) Sample vials and plates used on the platform. (C) Solid/powder dispensing in a balance chamber. (D) Press-filtration plate. (E) On-deck high-resolution camera. (F) On-deck nuclear magnetic resonance (NMR) sample tube holder. (G) 96-well microplate Reprinted with permission from Ref. [25]. Copyright 2023 Cell Reports Physical Science

In conclusion, the literature shows that automation technologies in electrochemistry – underpinned by advanced robotics and ML algorithms can greatly enhance reproducibility, accuracy, and efficiency in research. Integrating concepts of SDLs, especially in battery research, demonstrates automation's transformative potential. It allows researchers to explore chemical spaces and optimize systems at a pace and thoroughness that would be impossible to achieve manually. This background provides context for the present thesis, which illustrates a practical implementation of these principles in the development of a semi-automated system for cyclic voltammetry measurements. Our system integrates robotic pipetting for solution preparation, a modified 3D printer for precise electrode positioning, and a potentiostat for electrochemical data acquisition. As detailed in subsequent chapters, this semi-autonomous approach already achieves respectable improvements in throughput and

data consistency for electrochemical measurements. At the same time, the insights from the literature review highlight where our system can evolve further, for instance, by fully automating the control of the potentiostat and by incorporating real-time data analytics for decision-making. The ongoing shift towards fully automated, data-rich workflows in electrochemistry forms the foundation and motivation for our work, and the developments reviewed in this chapter show the remarkable progress that is guiding us towards genuinely self-driving electrochemical laboratories.

3. Theoretical Background

3.1 Principles of Cyclic Voltammetry (CV)

Cyclic voltammetry (CV) is a prominent electrochemical technique extensively employed to investigate electrochemical properties and electron-transfer behaviors of redox-active species. Its widespread use across disciplines such as chemistry, physics, and materials science results from its simplicity, versatility, and ability to rapidly characterize redox reactions.

In CV measurements, as outlined by Kissinger and Heineman (1983), the potential at a working electrode is systematically varied linearly over time between two predefined potential limits, known as switching potentials, forming a triangular waveform as shown in Figure 12. The current generated at the electrode surface is continuously measured as the potential is swept, creating a cyclic voltammogram—a graphical representation of current (y-axis) versus potential (x-axis).[26] This cyclic nature of potential sweeping, typically involving one or multiple cycles, allows a comprehensive investigation of oxidation and reduction processes within the same experiment, as further detailed by Elgrishi et al. (2018).[27]

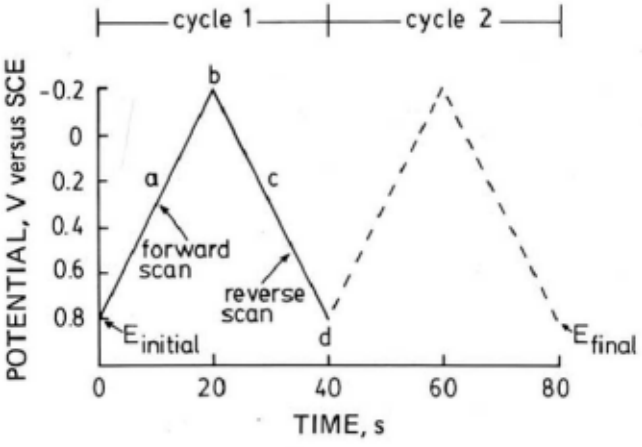

Figure 12. Typical excitation signal for cyclic voltammetry - a triangular potential waveform with switching potentials at 0.8 and -0.2 V versus a saturated calomel electrode (SCE). Reprinted with permission from Ref. [26]. Copyright 1983 American Chemical Society.

The distinctive "duck-shaped" (see Figure 13) curve of a cyclic voltammogram originates from the diffusion-controlled transport of electroactive species. As the potential is scanned negatively (cathodic sweep), oxidized species at the electrode surface are reduced, causing a rise in current. This leads to a cathodic peak, after which the current declines due to depletion of the reactant near the electrode, as diffusion becomes the limiting factor. When the scan is reversed (anodic sweep), the reduced species that have accumulated near the electrode surface are re-oxidized, resulting in an anodic peak. The symmetry and separation of these peaks offer insight into the reversibility and kinetics of the redox process. According to Kissinger and Heineman (1983), this peak-shaped current response arises because the current is directly proportional to the concentration gradient at the electrode surface, which initially increases but then diminishes as reactants are consumed. Thus, the characteristic voltammogram reflects not only the redox transformation but also the underlying mass transport dynamics that govern electron transfer processes.[26,27]

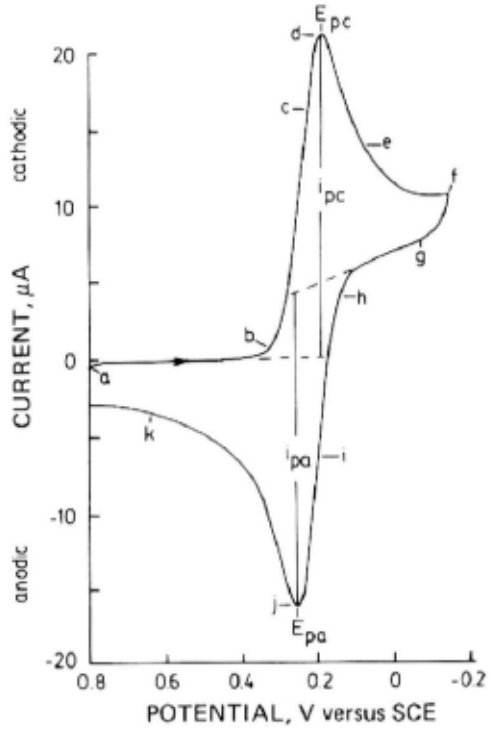

Figure 13. Cyclic voltammogram of 6 m*M* $K_3Fe(CN)_6$ in 1 *M* KNO_3. Scan initiated at 0.8 V versus SCE in negative direction at 50 mV/s. Platinum electrode, area = 2.54 mm^2. Reprinted with permission from Ref. [26]. Copyright 1983 American Chemical Society.

The separation of anodic and cathodic peaks provides valuable information about the reversibility of the electrochemical reaction. Kissinger and Heineman (1983) note that in an ideal, reversible electrochemical system, this peak separation closely matches theoretical predictions (typically around 59 mV/n, where n is the number of electrons involved). Detailed analysis of the voltammetry allows for example determination of fundamental parameters such as standard redox potentials and electron transfer rates.[26]

According to Elgrishi et al. (2018), the shape and magnitude of these voltammetric peaks are influenced by several critical parameters, including scan rate, electrode surface area, diffusion coefficients of electroactive species, and temperature. An increased scan rate results in a greater peak current due to faster depletion of species at the electrode surface yet can simultaneously widen the peak separation due to kinetic limitations.[27]

Chakrabarti et al. (2007) and Gursu et al. (2018) have demonstrated that in electrochemical energy storage applications, particularly in evaluating redox-active materials and electrolytes used in flow batteries, CV is instrumental in quickly screening and comparing electrochemical performance. It enables the selection of materials with desirable kinetics and redox potential, crucial for optimizing battery efficiency.[28–30]

3.2 Important Information Obtained from Cyclic Voltammetry

Building upon the significance of cyclic voltammetry (CV) in electrochemical research established in the preceding section, this section further elaborates on key features within cyclic voltammograms that provide crucial insights into the kinetics of electrochemical reactions and the properties of electroactive materials. The cyclic voltammogram generated in cyclic voltammetry (CV) contains several distinct features, each providing specific and essential insights into electrochemical processes. Researchers focus on varied characteristic features depending on the properties required, including peak current, peak current ratio, peak separation, and the

relationship between peak potentials and scan rates. These elements deliver critical information about the kinetics, mechanism, and reversibility of electrochemical reactions. Understanding these parameters facilitates deeper insight into the properties of electroactive materials and allows precise optimization for specific applications, including energy storage devices such as redox flow batteries (RFBs).

3.2.1 Peak Current versus Scan Rate

The peak current in cyclic voltammetry (CV) is one of the most fundamental parameters examined to elucidate electrochemical kinetics. It represents the maximum current observed during the electrochemical oxidation or reduction process and depends massively on the scan rate, defined as the rate at which the electrode potential is swept. According to the Randles–Sevcik equation, in diffusion-controlled electrochemical reactions, the peak current (i_p) exhibits a linear dependence on the square root of the scan rate ($v^{1/2}$), which is given by:

$$i_p = 0.4463nFAC(\frac{nFDv}{RT})^{1/2}$$

where *n* is the number of electrons transferred, *F* is the Faraday constant, *A* is the electrode's geometric area, *C* is the bulk concentration, *D* is the diffusion coefficient, *R* is the gas constant, and *T* is temperature.[31] This relationship implies that the current magnitude provides insights into both the diffusion coefficient and the number of transferred electrons . Thus, by examining how the peak current scales with scan rate, researchers can reduce these parameters if the reaction is diffusion controlled.

3.2.2 Peak Current Ratio

An effective diagnostic method for determining the reversibility of an electrode reaction is the ratio of the anodic to cathodic peak currents (i_{pa}/i_{pc}). In a reversible chemical reaction, the concentration of the reduced species after the forward scan is equal as the concentration of the reduced species before the CV. Thus theoretically, the ratio of the peak current (i_{pa}/i_{pc}).) is equal to one, and this value is independent of scan rate.[32] This ideal behavior indicates that the species produced during the

forward potential scan is quantitatively available for the reverse reaction on the following scan. However, a deviation from such ideal ratio is a clear sign that the electrode reaction mechanism is more complex than a simple reversible electron transfer. Typically, it suggests that the product of the initial electron transfer is unstable and is consumed by a coupled chemical reaction.[33]

3.2.3 Peak-to-Peak Separation

The separation between the anodic and cathodic peak potentials (ΔE_p) offers essential insights into the reversibility of an electrochemical reaction. A common approach for interpreting peak separation involves the Nicholson method[33], where the separation is related to a dimensionless kinetic parameter φ, reflecting the electron transfer rate constant (k^0) and diffusion coefficient. Practically, by systematically varying the scan rate and observing peak separation changes, researchers can estimate the kinetics of electron transfer and classify the electrochemical reaction, provided that the contribution of the uncompensated resistance is minimized. This method has been widely applied for electrode characterization and has proven valuable for materials used in energy storage devices, such as RFBs.[31]

In an ideal, reversible system, the peak-to-peak separation closely matches the theoretical value of approximately 59 mV/n at room temperature, signifying rapid electron transfer. Greater peak separations indicate quasi-reversible or irreversible systems, suggesting slower electron transfer rates. Randviir (2018) further clarified this relationship through experimental analysis of various redox-active species, emphasizing the practical application of ΔE_p in distinguishing between reversible, quasi-reversible, and irreversible reaction systems.

3.2.4 Diffusion Coefficient and Electrochemical Behavior

The relationship between peak potentials and the logarithm of the scan rate in cyclic voltammetry is instrumental in analyzing surface-confined redox reactions. The Laviron method is a well-established analytical tool used specifically for adsorbed

electroactive species, where diffusion does not govern electron transfer[34]. The Laviron equation relates peak potentials (E_p) to the scan rate (v) logarithmically and provides direct access to the electron-transfer kinetics (k^0) and the electron transfer coefficient (α) of the reaction.

In the Laviron analysis, deviations from linearity or variations in slope directly indicate changes in electron transfer rates or reaction mechanisms. For example, Lavagnini et al. (2004) successfully utilized this approach to determine kinetic parameters of adsorbed dopamine and hydroquinone, demonstrating precise quantification of electron-transfer rates. The strength of this method lies in its capability to elucidate subtle kinetic differences between surface-adsorbed species and diffusion-controlled systems, offering valuable insights into electrode surface modifications, crucial for optimizing electrode performance in electrochemical sensors and batteries. Though not applied in this work's analysis, understanding these methods provides context for evaluating electrode processes and could be applied in future studies

3.3 Electrode Positioning and its Role in High-Precision Measurements

Accurate and reproducible electrochemical measurements, particularly cyclic voltammetry (CV), depend dramatically on precise electrode positioning. Factors such as immersion depth, geometric area, and relative positioning of electrodes critically influence the reliability and accuracy of CV data. Thus, in designing a semi-autonomous system for CV measurement automation, great attention must be given to these parameters to ensure consistent results across multiple measurements.

The immersion depth of the cylindrical WE typically influences the effective geometric area available for electrochemical reactions. However, in standard electrode systems, only the bottom face of the WE serve as the active surface area, meaning immersion depth does not affect electrochemical reactions when the active bottom area is submerged. Conversely, in this project, the entire surface of the pencil graphite electrode acts as an active area. Thus, careful attention has been placed on

ensuring reproducibility by precisely controlling electrode positioning. Precise control over the immersion depth and positioning is vital because variations in these parameters can substantially alter the actual electrode surface area interacting with the electrolyte, thereby influencing the magnitude and reproducibility of measured electrochemical responses. Our automated, consistent positioning of the electrode ensures a stable and uniform interaction across measurements, significantly enhancing reproducibility and accuracy, and thus, is an essential component of this semi-autonomous electrochemical characterization system[35].

Another critical factor in achieving precise electrochemical measurements is the relative positioning of the reference electrode (RE) with respect to the working electrode (WE). Newman and Tiedemann (1993) demonstrated that placing the RE in close proximity to the WE significantly reduces errors stemming from ohmic potential drops, particularly important in regions of high and uniform current density. This arrangement enhances accuracy in determining electrode polarization characteristics and facilitates the identification of limiting electrodes during electrochemical measurements[35]. Hashibon et al. (2002) subsequently supported these findings, highlighting that optimal electrode configurations, specifically the close adjacency of RE to WE, minimize ohmic resistance and thus enhance measurement accuracy. They further noted the sensitivity of electrochemical measurements to even minor deviations in electrode placement, which can significantly influence measured overpotentials and current distribution[36].

In this project, we have optimized the semi-autonomous system by integrating a 3D printer as an electrode-positioning device, allowing precise adjustment of immersion depth. Additionally, the printed 3D electrode holder guarantees that the distance between the electrodes, particularly between the reference electrode (RE) and working electrode (WE), is fixed and identical for every measurement. By automating the movement and placement of electrodes, we remarkably reduce manual variability, enhancing both the accuracy and reproducibility of cyclic voltammetry results. This automated approach addresses the challenges highlighted by Zhang et al. (2014), who

underscored the necessity of minimizing ohmic drops by positioning the reference electrode outside the primary current pathway, thus providing accurate electrochemical measurements [37].

Finally, reproducibility across multiple wells is crucial in high-throughput CV experiments. Consistency in electrode positioning ensures that data collected from different wells are directly comparable. This comparability is crucial when investigating subtle differences in electrochemical responses across various samples. Our system addresses this challenge through standardized automated protocols, systematically applying almost identical electrode positions in each measurement cycle.

In summary, precise electrode positioning is fundamental to achieving high accuracy and reproducibility in cyclic voltammetry measurements. By leveraging automated positioning capabilities of a 3D printer and a precisely designed electrode holder, this semi-autonomous system significantly mitigates common positioning-related errors, ensuring robust and reliable electrochemical data.

4. Development of the Semi-Autonomous CV Measurement System

4.1 System Overview and Design Goals

The semi-automated cyclic voltammetry (CV) measurement system developed in this thesis comprises three integral components (see Figure 14): an automated liquid handling system (Opentrons OT-2 pipetting robot), a modified consumer-grade 3D printer (Prusa 3.5+) serving as a precision electrode positioning mechanism, and a PalmSens4 potentiostat for electrochemical data acquisition. Each component is carefully selected and integrated to minimize human involvement, thus enhancing the efficiency and reproducibility of electrochemical experiments.

The Opentrons OT-2 pipetting robot is specifically chosen due to its high volumetric accuracy and repeatability, markedly surpassing manual pipetting methods, thus ensuring consistent electrochemical sample preparation.

The modified Prusa 3.5+ 3D printer is selected because of its precise and programmable XYZ positioning capability. Equipped with a custom-designed three-electrode holder, it allows accurate and repeatable electrode positioning into each well of a standard laboratory wellplate.

The PalmSens4 potentiostat is integrated for its dependability, simplicity of interface through SDK, and demonstrated ability to deliver precise and steady electrochemical measurements

The design goal was to build a workflow in which a series of samples could be measured consecutively without requiring human involvement between measurements. The system is termed as "semi-autonomous" because, while mechanical operations are automated, the initiation of each CV and specific modifications, such as changing the working electrode and data processing, still require human intervention. Ultimately, the goal is to push the boundary closer to full autonomy by identifying and addressing any limiting steps.

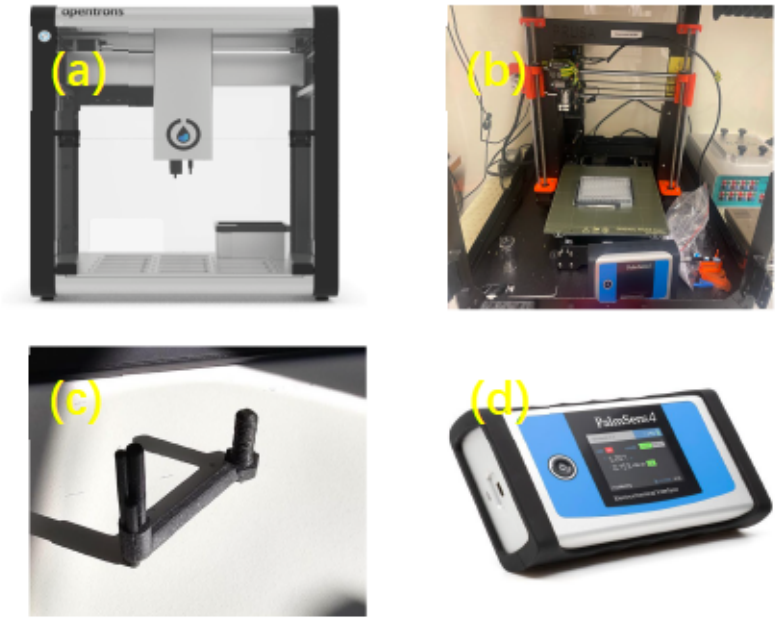

Figure 14. Components of the system (a) Opentrons OT-2 pipetting robot (b) Modified Prusa 3D printer with three-electrode holder (c) 3D printed holder for three-electrode system (d) PalmSens4 for CV measurements

4.2 Automated Solution Preparation with a Pipetting Robot

Consistent sample preparation is essential for any high-throughput experiment. We employed an Opentrons OT-2 liquid-handling robot to automate the preparation of redox-active solutions for CV measurements. The robot was programmed (using Opentrons Protocol Designer) to dispense precise volumes of stock solutions, metal salt, ligand, and supporting electrolyte, into each well of a 96-well plate. This automated dispensing ensures improved volumetric accuracy and parallel preparation of multiple samples, eliminating errors associated with manual pipetting. Moreover, the robot could mix the dispensed reagents by aspirating and dispensing, ensuring homogeneity across samples before measurements.

In our workflow, each well was prepared to contain an iron–ligand complex at defined concentrations in a strongly basic supporting electrolyte (see Figure 15). For example, to screen various ligands' effects on the Fe(III)/Fe(II) redox couple, the robot dispensed iron(III) chloride and a given ligand (e.g., TAPSO, BIS-TRIS propane, Tricine, triethanolamine (TEA), or DIPSO) along with a high-pH supporting electrolyte into the well. Each 100 µL sample was formed *in situ* under controlled

concentration and pH conditions, enabling direct comparison of electrochemical behavior between different Fe–ligand complexes. Specifically, 20 µL of an $FeCl_3$ stock solution (0.2 M) was added to each well, providing a final Fe^{3+} concentration of 0.04 M. Next, 40 µL of a ligand stock solution (0.25 M) was added, yielding a 0.10 M final ligand concentration. To establish a highly basic medium, a total of 40 µL of strong base was then added as the supporting electrolyte. This consisted of 20 µL of 0.2 M NaOH and 20 µL of 0.2 M KOH, which were combined in the well. The supporting electrolyte was thus composed of NaOH and KOH (each at 2 M in their stock solutions), ensuring a strongly alkaline environment (combined $[OH^-] \approx 0.08$ M in the well, corresponding to pH ~13–14). These conditions (summarized in Table 1) were chosen to maintain Fe(III) in a hydrolyzed but soluble state and to promote complex formation with the ligands at high pH. The OT-2 robot's protocol standardized the order and timing of additions: after dispensing all components (Fe^{3+} source, ligand, NaOH, KOH), the robot performed a gentle mixing and a brief incubation to allow complexation equilibrium to be reached in each well. This automated, uniform preparation minimized variability, each well experienced the same handling, mixing, and waiting period, which is crucial for reliable high-throughput CV measurements.

Table 1. Composition of each 100 µL sample well

Component	**Stock Concentration**	**Volume per well**	**Final Concentration in well**
$FeCl_3$	0.2 M	20 µL	0.04 M (Fe^{3+})
Ligand (e.g., TAPSO)	0.25 M	40 µL	0.10 M
NaOH	0.2 M	20 µL	0.04 M (NaOH)
KOH	0.2 M	20 µL	0.04 M (KOH)
Total	-	100 µL	pH ~ 13-14

2

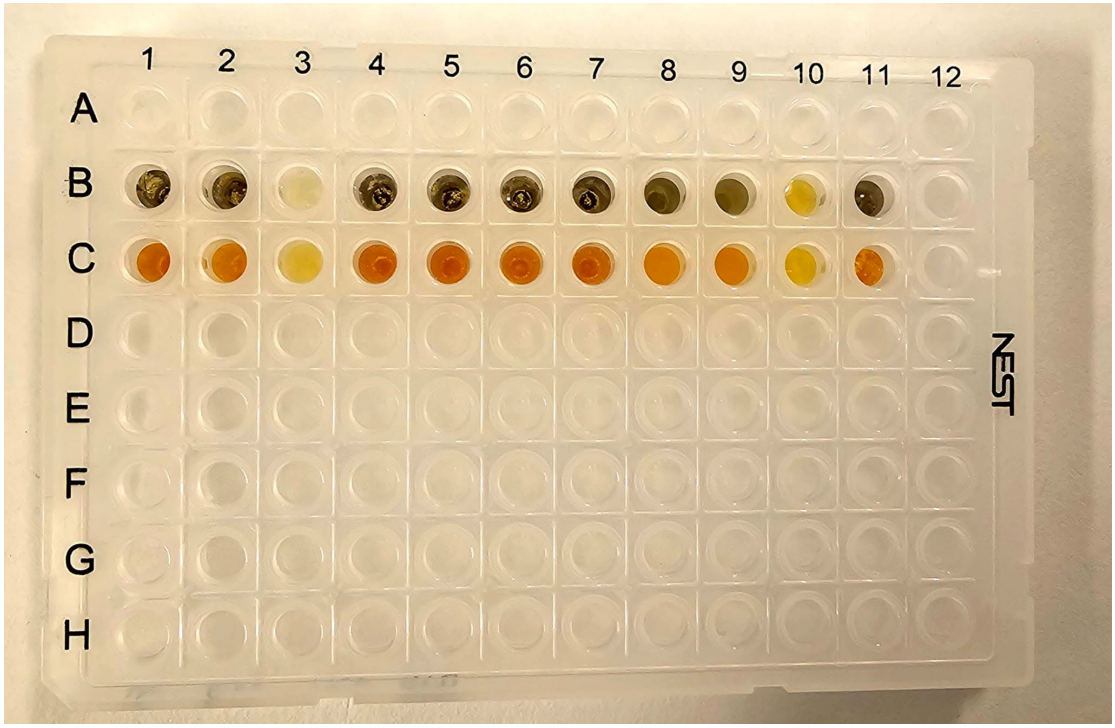

Figure 15. Iron complexes with different ligands

This highly basic supporting electrolyte (prepared by combining concentrated NaOH and KOH solutions) ensured that the Fe(III)–ligand complexes were studied in a reproducible, strongly alkaline environment. The strong bases provides a consistent ionic background for voltammetric measurements. By automating the solution preparation in this manner, the system achieved excellent consistency. Each well received identical reagent amounts and experienced the same mixing protocol. Consequently, any differences observed in the electrochemical responses can be attributed confidently to the differing ligands rather than to sample preparation errors. The result of this automated preparation step was a well-plate pre-loaded with a series of Fe–ligand complexes at uniform concentrations and high pH, ready for electrochemical analysis. The plate was then transferred to the modified 3D-printer-based electrode positioning system for CV measurements (as described in Chapter 4.3), with the well positions calibrated in advance to ensure precise electrode immersion depth in each 100 µL solution.

4.3 Modified 3D Printer for Electrode Positioning

A key innovation in this project is repurposing a consumer-grade Prusa 3.5+ 3D printer as a robotic positioning system for the electrodes. The Prusa 3.5+ is a popular fused-filament fabrication (FFF) printer with stepper motor control in X, Y, and Z axes and firmware that accepts standard G-code instructions. We removed the filament extruder assembly and replaced the print head with a custom 3D-printed electrode holder. This electrode holder was designed using CAD software to fit into the space where the printer's nozzle assembly was, attaching firmly to the printer's X-axis carriage. One practical modification to the printer was the removal of the nozzle heater and disabling the extrusion motor. This eliminated any risk of the controller trying to heat or extrude (which could damage our holder or cause unnecessary movement). The firmware was configured in a "dry run" mode since we only needed motion control.

A custom three-electrode holder was designed using a CAD model created in Shapr3D, specifically tailored for compatibility with the Prusa 3.5+ printer. The well plates used in this experiment had small diameter, requiring the holder to be designed with precise dimensions, as shown in Figure 16, the scale of the design was reduced to the millimeter level, with each electrode measuring approximately 1mm in diameter or even smaller due to filleted edges for improving printing quality.

The holder needed to securely mount three electrodes (working, reference, counter) in a fixed geometry. I designed it to accommodate a pencil graphite rod (0.5 mm diameter mechanical pencil lead, 60 mm length) as the working electrode, a leak-free Ag/AgCl reference electrode (a small, sealed reference, about 6 mm diameter, often used in portable devices), and a Pt wire counter electrode (0.5 mm diameter, bent into a small loop). The holder has three channels to hold each electrode at a specific relative position. The entire assembly's footprint is small enough to fit into a single well plate without touching the sides. Because each well in a standard plate is about

16 mm in diameter, and our electrodes are about 1 mm thick or less, the holder was roughly 10 mm in diameter.

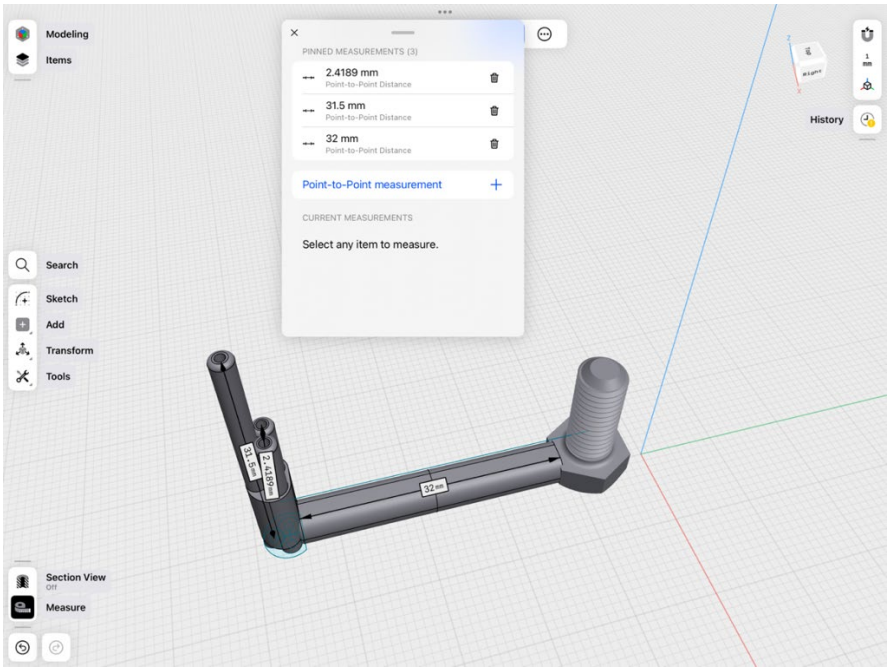

Figure 16. Design of three-electrode system

The printing of this model demanded fine resolution. The final design included features like small, filleted edges and tight tolerances to grip the electrodes firmly. I iterated the design a few times – early prototypes either didn't hold the electrodes tightly enough or were too bulky, interfering with the well. One challenge I encountered was attaching the holder to the printer's existing hardware. I ended up utilizing the screw holes from the removed nozzle and designing the holder with a matching bolt pattern, allowing it to be screwed into the heater block of the Prusa's hotend as shown in Figure 17. As a result, the electrodes now effectively replaced the nozzle in the printer's coordinate system. So additionally, the model also included a bolt design that allowed the electrode holder to screw into the heater block. A 32 mm bridge was included to ensure the holder's stability and alignment. This model was first printed by Prusa 3.5+ using Polylactide (PLA), which initially served as the primary printer for fabricating the electrode holder. However, the final models were successfully printed using a Bambu printer. Once the final model was successfully printed using the Bambu printer, the three-electrode holder was assembled into the modified Prusa 3.5+. This step completed the transformation of the Prusa printer into

an electrode positioning machine, enabling precise control of the electrodes during experiments.

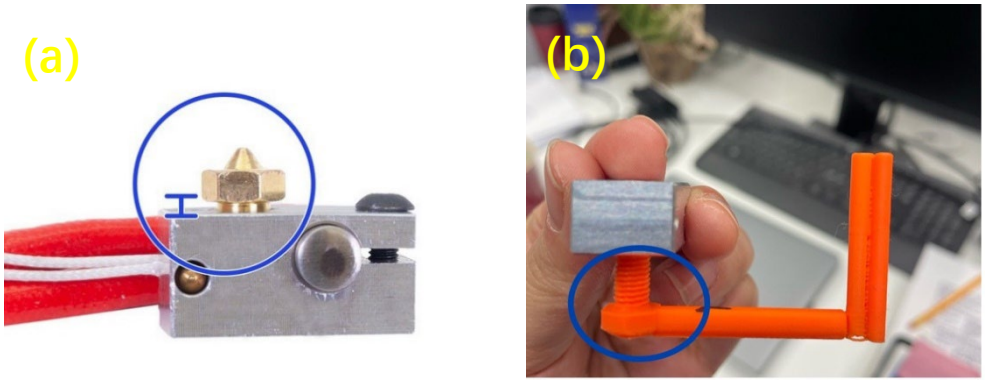

Figure 17. Nozzle replacement (a) Heater block with original nozzle (b) Heater block with three-electrode holder

4.4 G-code for Electrode Positioning

By sending G-code commands via a connected computer, the printer's firmware was used in relative motion mode. The coordinate system was calibrated so that a specific XYZ coordinate corresponded to a given well position and a desired electrode immersion depth. For example, positions like (X=22, Y=136) was determined to align the electrodes with the center of well A1. A small script was written to generate the sequence of G-code moves needed: move to above a well (at a safe Z height), then lower Z into the solution, wait for the CV to run, raise back up, possibly move to a rinse station, etc. An excerpt of the G-code is provided in the Appendix, showing the approach to each well and timed delays. I included a corner position (X=20, Y=140, Z=150) which is a spot away from any wells; the system moves there between measurements as a home base. I also designated multiple wells as cleaning wells containing a rinsing solution. After each measurement, the electrodes were dipped in the cleaning well to mitigate cross-contamination between samples (with a wait period to allow diffusion of any residues).

The stepper motors of the Prusa printer have a typical resolution of 0.01 mm in X–Y and even finer in Z, which is more than adequate. However, backlash and mechanical

play can reduce effective accuracy. I mitigated this by always approaching coordinates from the same direction (in G-code, moving in a consistent pattern so slack is taken up in one direction) and moving slowly for the final approach to a position. We also tested repeatability by commanding the printer to dip into a well of plain water multiple times and measuring the actual depth the working electrode reached. The variation was within ±0.1 mm, which gave us confidence that each CV run was done at essentially the same immersion depth.

4.5 Electrochemical Measurement with PalmSens Potentiostat

For the electrochemical measurements, we used a PalmSens4 potentiostat connected to the three electrodes via a small cable bundle running along the printer's arm. The PalmSens4 is a portable potentiostat capable of performing cyclic voltammetry and other techniques, and it interfaces with PC software (PalmSens PSTrace) for control and data logging. In our semi-automated setup, starting a CV scan still requires a software trigger. We achieved a semi-automated workflow by synchronizing the G-code sequence with the potentiostat operation in time. Specifically, our G-code would move the electrodes into a well and then include a delay (e.g., wait 5 seconds) during which we manually initiated the CV scan in the PSTrace software. Once the scan (which typically took a few seconds for the potential sweep) was finished and the data were recorded, the G-code delay would end and the printer would automatically retract the electrodes and move to the next position.

To eventually remove even that manual step, we explored the PalmSens SDK, which allows external programs to control the potentiostat. A future iteration of this project could use a single Python script to send a command to start the CV scan at the right moment (for example, a trigger when the Z position is reached). However, in the present work, the semi-automated approach was sufficient to demonstrate the concept: the electrodes moved themselves from sample to sample, and the experimenter only had to click a button to start each scan.

The CV parameters were kept constants for all measurements to ensure comparability:

a potential window from 0 V to –0.8 V (vs Ag/AgCl) and back, at a scan rate of 50 mV/s, was used for the iron complexes studied. These parameters were chosen based on the known chemistry of the Fe(III)/Fe(II) couples (which are expected to be in the –0.1 to –0.6 V vs Ag/AgCl range for the ligand types we used). Additionally, using a moderate scan rate at 50 mV/s strikes a balance between signal-to-noise and experiment speed for high-throughput work. Too slow a scan rate would make each measurement longer (lower throughput), and too fast could distort peak shapes if the system has any residual uncompensated resistance or if the electron transfer kinetics are borderline.

During each CV run, the PalmSens recorded the current vs potential data, which were saved to disk with filenames corresponding to the sample ID. Immediately after each run, basic data (such as peak currents and peak potentials) were extracted by the software's built-in analysis. The potentiostat's compliance voltage and current range were adequate for the small-scale cells; typical currents we observed were in the tens of microamps, well within PalmSens4's capabilities.

One issue encountered was electrical noise when the printer motors were active. When a motor moves, it can generate electrical noise that might couple into the potentiostat leads. To avoid measurement interference, we ensured that the motors were idle during the actual CV scan (hence the pause in G-code).

The electrochemical measurement component provided the necessary data collection, and while it required some manual synchronization in this iteration, it is poised for full automation with minor additional programming. With the system fully assembled pipetting robot for setup, 3D printer for electrode handling, and a potentiostat for measurement, we proceeded to validate its performance.

4.6 Difficulties and Challenges in System Development

Throughout the development of the semi-autonomous CV measurement system, several prominent challenges were encountered, primarily linked to the modification

and optimization of the Prusa 3D printer and the design of the three-electrode holder.

One of the primary issues that arose during the design phase of the electrode holder was the dimension. Determining the optimal diameter of the holder tubes was challenging due to the inherent properties of 3D printing filament, which experiences thermal expansion and contraction during heating and cooling cycles. This thermal variability led to inconsistent tube diameters, tremendously affecting the precision and reliability of electrode placement. Additionally, ensuring structural integrity was complicated, as thinner models were prone to breakage. To mitigate these problems, numerous iterations were necessary, systematically adjusting parameters such as layer height, infill density, print speed, and support structures. Each of these parameters profoundly influenced the quality of the printed models, and inadequate tuning in any aspect could lead to printing failures, exemplified by failed prototypes illustrated in Figure 18.

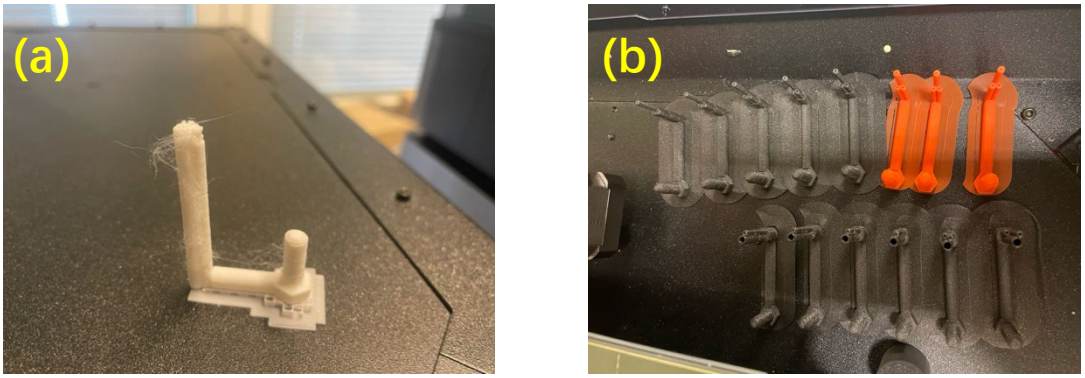

Figure 18. Iterations of the design. (a) Failed model due to insufficient printing time (b) Models with varied size

A second critical challenge involved designing the screw component that attaches the custom electrode holder to the extruder of the Prusa printer. Precise specifications for the original extruder screws were not publicly available, posing significant difficulties in designing the CAD model for the new electrode holder system. Achieving a screw with exact spiral dimensions to ensure a secure and stable connection proved highly problematic. After extensive trial-and-error experimentation, a functional yet imperfect set of dimensions was identified. Although this solution allowed the continuation of the project, the dimensions were not ideal, and the time constraints

limited further optimizations, resulting in the acceptance of this suboptimal design.

Operational issues are also presented during the measurement phase. The Prusa printer operates with pre-programmed default coordinates that positioned the three-electrode holder dangerously close to the printing plate. In some instances, once the printer-initiated movement towards these default positions, no subsequent command could halt this potentially damaging action. This flaw resulted in physical damage, including the snapping of the holder screw and partial obstruction of the extruder mechanism. To address this issue, custom "home coordinates" were defined within the G-code sequences, instructing the printer to move safely away from the well plate after each measurement, thereby preserving the integrity of the experimental setup and equipment.

A related problem emerged due to subtle movements of the substrate supporting the well plate whenever the printer shifted to different measurement coordinates. Even minor shifts posed risks of cross-contamination among solutions and inaccuracies in recorded positions. To resolve this, additional walls (see Figure 19) were printed and strategically positioned around the well plate. These stabilizing walls were affixed securely to the printing plate, effectively maintaining the position of the well plate and ensuring the high accuracy and reproducibility of data. Importantly, these fixtures were designed to be removable without causing damage to the printing plate.

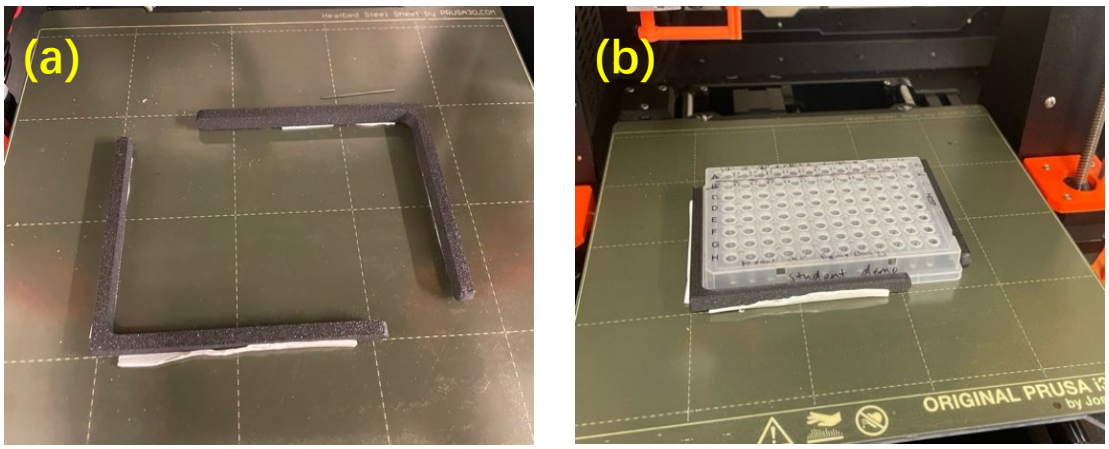

Figure 19. Wellplate with walls

These difficulties encountered underscore the intricate considerations necessary when

integrating commercial 3D printers into precise laboratory setups. Each challenge required methodical troubleshooting and iterative optimization, reflecting broader issues inherent in transitioning laboratory automation from semi-autonomous to fully automated systems. Future improvements could benefit significantly from comprehensive documentation and standardized specifications provided by equipment manufacturers, alongside continued refinements in custom design parameters.

4.7 Comparative Analysis of Automated Cyclic Voltammetry Systems

To fully appreciate the advancements and unique advantages of the developed semi-autonomous cyclic voltammetry (CV) measurement system, it is valuable to position it in the broader context of automated electrochemical research systems. Several automated platforms for electrochemical characterization and materials discovery have emerged, each addressing unique challenges and incorporating distinct methodological approaches.

The ECARUS platform (detailed in Section 2.1.2), focuses mostly on solution-phase synthesis with no distinct emphasis on electrode handling accuracy, despite its remarkable performance in autonomous synthesis and optimization tasks using machine learning methods. In contrast, our system prioritizes precision and reproducibility in electrode placement, directly improving the quality and consistency of electrochemical data.

Unlike the ORGANA robotic system (detailed in Section 2.2.1), which is versatile in handling various chemistry experiments but lacks specialized provisions for electrochemical analyses, our system specifically excels in automated cyclic voltammetry through precise electrode positioning and accurate solution preparation. Our approach addresses the niche yet critical needs of electrochemical measurements directly.

In the context of electrochemical research, the "Electrolab" platform developed by Oh et al. (2023) is particularly relevant (see Figure 20). This modular platform automates

redox-active electrolyte characterization using microfabricated electrode arrays, a multiplexer, and Python-controlled robotics.[21] Despite similarities in automation and electrochemical focus, their system primarily targets batch voltammetric experiments without precise 3D-printed electrode holders or electrode positioning. The advanced flexibility and customizability of our modified Prusa 3D printer system, capable of precise, programmable electrode positioning, represents a substantial improvement in ensuring repeatable and high-quality CV measurements.

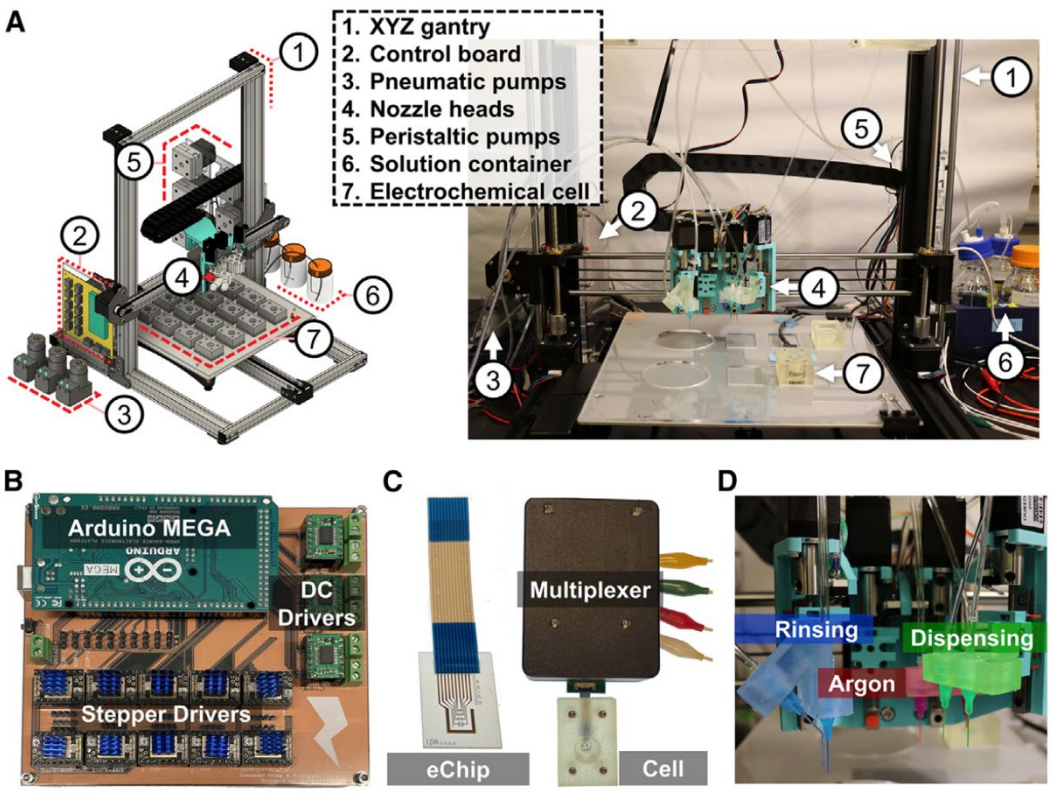

Figure 20. Hardware modules of the Electrolab (A) 3D model of the Electrolab solution-handling robot and the fully assembled robot with labeled components. (B) Universal electromechanical control board with an Arduino Mega microcontroller, DC drivers, and stepper motor drivers. (C) Components of the electrochemical module: microfabricated eChip electrode arrays, the electrochemical cell, and the multiplexer that selects between the different electrodes. (D) Fluidic nozzle system mounted on the XYZ gantry, with all nozzles able to be moved up/down individually. Nozzles are responsible for dispensing and disposing of fluids, rinsing and flushing with solvent, and drying or sparging with argon. Reprinted with permission from Ref. [21]. Copyright 2023 Elsevier.

Systems discussed by Chen et al. (2024) and Pence et al. (2025) highlight digitalization and automation in redox-flow battery experimentation.[38,39] In

comparison, our system adds two key innovations: (1) a robust, automated electrode-positioning mechanism, and (2) a flexible 3D-printed electrode holder design. These address a critical but often overlooked challenge in electrochemical automation, which is the precise and reproducible electrode placement.

Thus, while existing systems individually address aspects such as synthesis optimization, rapid prototyping, or general electrochemical automation, the comprehensive integration of automated solution preparation, precise electrode positioning, and consistent cyclic voltammetry measurements presented in this thesis represents a revealing advancement. This holistic approach not only improves experimental reproducibility but also positions the system as an innovative solution in the high-throughput electrochemical characterization and materials discovery landscape. The next chapter presents the results from testing this semi-autonomous system on a set of iron coordination complexes, demonstrating the data quality, reproducibility, and insights gained, as well as areas for improvement identified through this process.

5. Results and Discussion

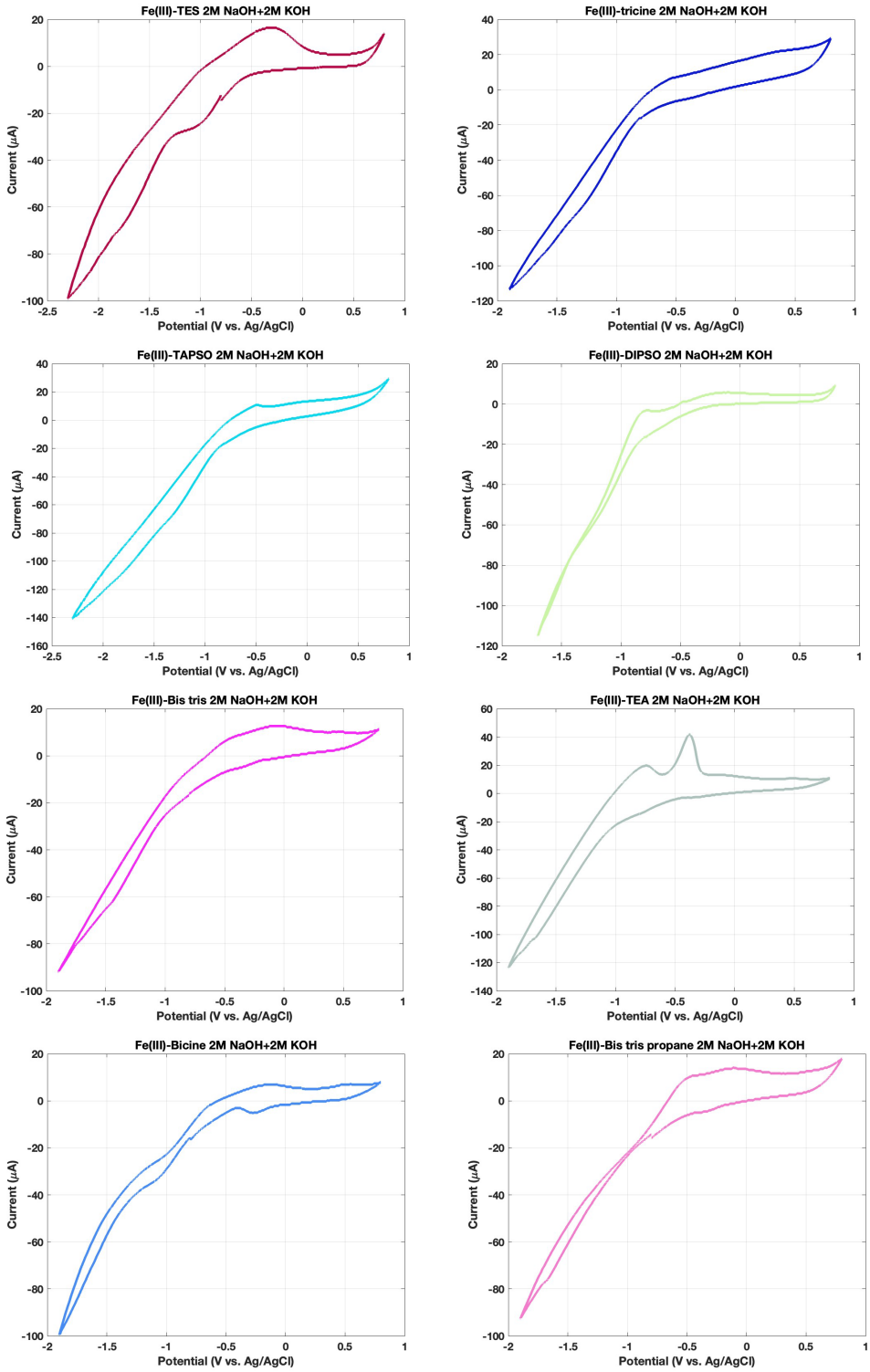

Figure 21. Electrochemical characterization of Iron complexes using semi-automated CV setup

5.1 CV Measurements of Iron Redox Complexes

The cyclic voltammetry measurements were conducted using a three-electrode setup consisting of pencil graphite (0.5 B, Ain STEIN, 0.5 × 60 mm) as the working electrode, a leak-free Ag/AgCl reference electrode, and a Pt wire counter electrode. Iron-based complexes were selected for this study due to their promising application in redox flow batteries (RFBs), which are attractive alternatives to vanadium-based batteries because of their higher sustainability, lower toxicity, and cost-effectiveness. Iron complexes offer advantages such as high solubility in aqueous solutions, desirable electrochemical stability, and versatile redox potentials, aligning well with the criteria for efficient energy storage materials[40]. Using this configuration, the CV measurements were performed with the PalmSens4 potentiostat. The results of these experiments are presented in Figure 21.

5.2 Results Analysis

The automated CV measurements demonstrated that three of the tested Fe–ligand complexes (TAPSO, BIS-TRIS propane, and Tricine) yielded well-defined redox peaks at potentials consistent with conventional three-electrode results. This congruence confirms that the semi-automated setup is capable of accurately capturing the fundamental electrochemistry of Fe(III)/Fe(II) couples for suitable ligand environments. Conversely, the complexes with TEA and DIPSO exhibited attenuated or disrupted voltammetric responses in ambient conditions, specifically, Fe–TEA showed an unexplained extra peak (~ –0.37 V) and Fe–DIPSO's main redox peak was largely lost without inert gas. These differences underscore the influence of experimental conditions (like atmospheric oxygen) and ligand chemistry on the observed electrochemical behavior. It is also worth noting that all five complexes showed relatively low peak currents. This is expected given the small 0.5 mm pencil graphite working electrode and the moderate concentration (0.04 M Fe). The peak intensities, while sufficient to identify redox processes, were not very large, indicating that using a larger-area or more conductive working electrode, or increasing the

timescale for diffusion could improve the signal-to-noise ratio. Indeed, prior studies recommend using stable electrodes like glassy carbon electrodes for reproducible CV measurements, as they provide more consistent responses over time[41].

Despite this, the trends and features for each complex were reproducibly obtained across multiple wells, illustrating the reliability of the robot-prepared samples and automated electrode positioning. Overall, the results analysis confirms that the semi-autonomous system can discern meaningful differences in redox behavior attributable to ligand effects, while also highlighting areas for improvement (such as inert atmosphere control and electrode enhancements) to better resolve certain complexes' electrochemistry.

6. Conclusion and Future Work

This thesis has successfully demonstrated the development of a semi-automated system for cyclic voltammetry, integrating robotic solution preparation and precise electrode positioning to achieve high-throughput electrochemical measurements. The core accomplishment is the seamless coupling of an Opentrons OT-2 pipetting robot with a modified Prusa 3D printer-based three-electrode setup and a PalmSens4 potentiostat, thereby automating the traditionally labor-intensive steps of sample preparation and data acquisition. By reducing human involvement at these stages, the system markedly improved reproducibility and throughput.

The automated liquid handling ensured that every iron–ligand sample was prepared with identical concentrations and under the same strongly basic conditions, effectively eliminating pipetting variability. Likewise, the custom 3D-printed electrode holder mounted on the printer delivered consistent immersion depth and alignment for each measurement. As a result, the cyclic voltammetry (CV) data obtained were more consistent and reliable compared to those from fully manual experiments. The successful detection of Fe(III)/Fe(II) redox peaks for multiple iron–ligand complexes validated the system's functionality. In particular, complexes such as Fe–TAPSO, Fe–BIS-TRIS propane, and Fe–Tricine showed redox potentials in the automated setup that matched those from conventional experiments, confirming that the instrumentation did not distort the electrochemical responses. This agreement with expected results underscores the effectiveness of the semi-automated approach in maintaining control over experimental conditions.

At the same time, the work has shed light on several limitations and challenges that remain. The use of pencil graphite leads as working electrodes, while convenient for prototyping, introduced issues due to their mechanical fragility and variable surface properties. Electrodes occasionally broke during insertion or measurement, interrupting the workflow and necessitating manual replacement, a clear bottleneck for true high-throughput operation. Additionally, although the robot and printer

automated most steps, the initiation of each CV scan still required manual intervention via the potentiostat software, highlighting an opportunity for further integration. Another challenge was observed in the electrochemical results for certain complexes (e.g., Fe–TEA and Fe–DIPSO): dissolved oxygen and other environmental factors interfered with the redox signals in the absence of an inert atmosphere. The diminished or lost peaks in those cases emphasized that without environmental control, the platform may not capture the full electrochemistry of oxygen-sensitive systems. Finally, the physical constraints of the hardware became apparent. For instance, the standard 96-well plate geometry and the 3D printer's default Z-axis homing position were not perfectly aligned, leading to situations where electrodes could penetrate too deeply into wells or collide with the well bottom if not carefully calibrated. These issues occasionally resulted in electrode damage or suboptimal positioning, affecting data quality. In summary, while the semi-automated system advances laboratory CV automation, these identified shortcomings must be addressed to realize a fully robust and autonomous experimental platform.

To overcome the current limitations and build upon the findings of this research, several key future developments are proposed. Each recommendation directly stems from the challenges encountered and the insights gained in Chapters 2–5, aiming to elevate the system's performance and autonomy:

Full Automation of Potentiostat Operation: The remaining manual step of initiating and controlling the CV scans can be eliminated by integrating the PalmSens4 potentiostat with the robotic system through software. For example, using the PalmSens Software Development Kit (SDK) in a Python-based control program would allow automated triggering of measurements and real-time data logging. This improvement would synchronize the 3D printer's electrode positioning with the potentiostat's operation, enabling truly hands-free execution of sequential scans. By removing the need for a human operator to start each run, we reduce the potential for timing inconsistencies and human error, thereby enhancing both throughput and reproducibility.

Robust Electrode Materials and Custom Wellplate Design: To address the fragility and inconsistency of the pencil graphite working electrodes, future iterations of the system should employ more durable electrode materials such as glassy carbon or other carbon-composite electrodes. Glassy carbon, in particular, is well-known for its mechanical stability and reproducible surface properties, making it ideal for reliable CV measurements over many cycles.[41] Using a robust electrode will prevent frequent breakage and ensure stable performance across hundreds of automated measurements. In tandem with better electrodes, a customized wellplate is needed to accommodate the new setup. As shown in Figure 22, we have begun designing a 3D-printed wellplate that incorporates a planar carbon working electrode as part of each well. In this design, each well's bottom would be hollow and sealed with a conductive carbon sheet (or a thin glassy carbon plate), which serves as the working electrode for that well. Such a configuration would effectively embed a durable electrode into the plate, eliminating the need to physically insert and replace pencil leads. This custom plate can be made taller or altered geometry to fit the 3D printer's coordinate system. For instance, a slightly elevated well height will ensure the printer's Z-axis movement positions the electrodes correctly without pressing them against the well bottom (resolving the prior z-axis clearance issue). We also plan to integrate the stabilizing features (the 3D-printed support "walls") into the plate design itself so that the plate can be securely fixed on the printer platform during operation. Overall, by introducing a purpose-built wellplate with built-in robust electrodes, we aim to vastly improve the system's reliability and ease of use: the electrode alignment will remain consistent by design, and the fragility issue of graphite leads will be eliminated, thereby streamlining high-throughput experiments.

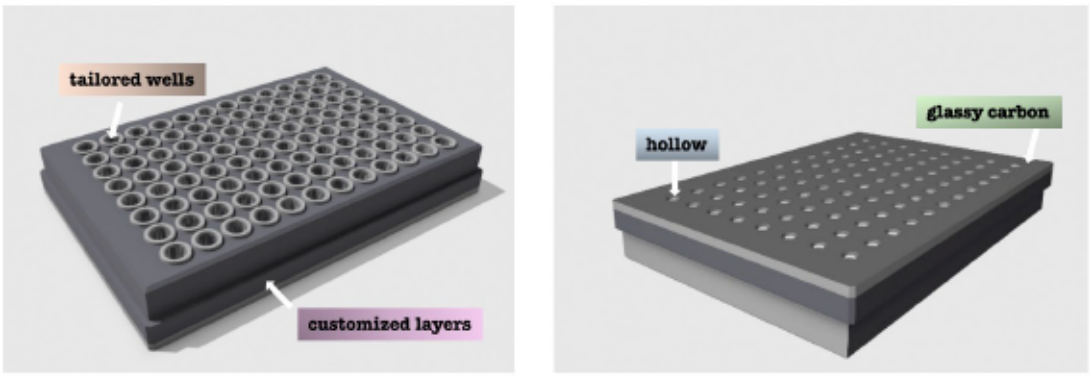

Figure 22. Custom wellplate design

Enhanced Environmental Control: Results from Chapter 5 highlighted that some Fe–ligand redox signals were compromised by the presence of dissolved oxygen. Therefore, implementing an inert atmosphere or gas purging mechanism is a crucial next step. Enclosing the CV setup in a small environmental chamber or glovebox and purging with nitrogen (or argon) during measurements will significantly reduce O_2 interference. This improvement is expected to yield clearer and more defined voltammograms, particularly for oxygen-sensitive complexes like Fe–DIPSO and Fe–TEA, whose redox chemistry was not fully observable under ambient conditions. By ensuring an oxygen-free environment, we can better capture the true electrochemical behavior of a wider range of analytes. This modification ties back to observations in our experiments and aligns with standard electrochemical practices for sensitive systems. Introducing controlled atmosphere capabilities will broaden the scope of the semi-automated system, allowing exploration of redox chemistry that was previously masked by air effects, and thus making the platform more versatile for research on air-sensitive redox catalysts or anaerobic processes.

Adaptive Experimentation Using Machine Learning: While the current work focused on hardware and process automation, future efforts could integrate machine learning (ML) algorithms to make the system smarter and more autonomous in experimental decision-making. Building on the concepts discussed in Chapter 2 (regarding self-driving labs and AI-driven optimization), we envision implementing a real-time data analysis and feedback loop. For example, preliminary CV data from a

series of runs could be analyzed on-the-fly to inform the selection or modification of subsequent experimental parameters (such as scan rate, concentration, or ligand structure for the next set of experiments). By using ML models trained on CV results, the system could adaptively optimize conditions to enhance signal quality or explore promising regions of chemical space without human input. This approach would accelerate discovery where the robot could iteratively hone in on the most interesting redox-active complexes or optimal conditions (e.g., identifying which ligand leads to the most reversible Fe redox couple, then testing similar ligands or varying pH around that system). Such adaptive experimentation transforms the setup from a static high-throughput screener into a dynamic self-driving laboratory capable of learning from results in real time, a direction that represents the cutting edge of automated chemistry.

Expanded Application to Diverse Electrochemical Systems: Finally, future work should extend the use of the semi-automated platform beyond the specific iron–ligand complexes studied here. The fundamental design, automated solution handling and electrode positioning, is quite general and can be applied to other redox-active systems in energy research and catalysis. By validating the system with different electrochemical scenarios (for instance, screening battery electrolyte additives, analyzing coordination complexes of other metals, or studying pH-dependent molecular electrocatalysts), we can demonstrate its robustness and versatility. Each new application may pose unique challenges (different solvent systems, need for reference electrode calibration, etc.), but overcoming those will further prove the platform's utility. In particular, examining faster or more complex electron-transfer reactions would test the system's temporal and spatial precision, and integrating different detection modes (e.g., alternating current voltammetry or electrochemical impedance spectroscopy) could broaden its functionality. The ultimate goal of these expansions is to establish the semi-automated CV system as a widely applicable tool for accelerating electrochemical research, capable of generating high-quality, reproducible data across a spectrum of chemical inquiries.

In summary, this work represents a suggestive step toward fully autonomous electrochemical experimentation. The semi-automated CV system enhanced experimental consistency and throughput by combining robotics with electrochemical analysis, aligning well with the emerging paradigm of self-driving laboratories. By explicitly addressing the challenges encountered, from electrode material limitations and mechanical design constraints to the need for software integration and environmental control, we have charted a clear path for future improvements. Implementing the proposed solutions will move the system closer to a turn-key, robust platform that not only runs experiments without human intervention but also intelligently adapts and extends to new problems. Such advancements are poised to deliver faster, more accurate, and more insightful electrochemical data, which is invaluable for accelerating progress in energy storage, catalysis, and beyond. Ultimately, the lessons learned, and the innovations developed in this thesis lay the groundwork for next-generation automated electrochemical setups, bridging the gap between traditional manual experimentation and the autonomous labs of the future.

References

[1] G. Tom, S. P. Schmid, S. G. Baird, Y. Cao, K. Darvish, H. Hao, S. Lo, S. Pablo-García, E. M. Rajaonson, M. Skreta, N. Yoshikawa, S. Corapi, G. D. Akkoc, F. Strieth-Kalthoff, M. Seifrid, A. Aspuru-Guzik, *Chem. Rev.* **2024**, *124*, 9633.

[2] S. Pablo-García, Á. García, G. D. Akkoc, M. Sim, Y. Cao, M. Somers, C. Hattrick, N. Yoshikawa, D. Dworschak, H. Hao, A. Aspuru-Guzik, *Device* **2025**, *3*, 100567.

[3] J. Li, Y. Tu, R. Liu, Y. Lu, X. Zhu, *Adv. Sci.* **2020**, *7*, 1901957.

[4] L. Gundry, S.-X. Guo, G. Kennedy, J. Keith, M. Robinson, D. Gavaghan, A. M. Bond, J. Zhang, *Chem. Commun.* **2021**, *57*, 1855.

[5] A. Mistry, A. A. Franco, S. J. Cooper, S. A. Roberts, V. Viswanathan, *ACS Energy Lett.* **2021**, 1422.

[6] B. P. MacLeod, F. G. L. Parlane, A. K. Brown, J. E. Hein, C. P. Berlinguette, *Nat. Mater.* **2022**, *21*, 722.

[7] V. Shkirskiy, F. Kanoufi, *Curr. Opin. Electrochem.* **2024**, *46*, 101526.

[8] L. Nejdl, J. Kudr, B. Ruttkay-Nedecky, Z. Heger, L. Zima, L. Zalud, S. Krizkova, V. Adam, M. Vaculovicova, R. Kizek, *Int. J. Electrochem. Sci.* **2015**, *10*, 3635.

[9] T. Erichsen, S. Reiter, V. Ryabova, E. M. Bonsen, W. Schuhmann, W. Märkle, C. Tittel, G. Jung, B. Speiser, *Rev. Sci. Instrum.* **2005**, *76*, 062204.

[10] S. Kamran Haghighi, S. Mohammadlou, S. Angizi, A. Hatamie, *Langmuir* **2025**, *41*, 8592.

[11] K. Laws, M. Tze-Kiat Ng, A. Sharma, Y. Jiang, A. J. S. Hammer, L. Cronin, *ChemElectroChem* **2024**, *11*, e202300532.

[12] D. Chaos, J. Chacón, J. Lopez-Orozco, S. Dormido, *Sensors* **2013**, *13*, 2595.

[13] A. Kantaros, C. Drosos, M. Papoutsidakis, E. Pallis, T. Ganetsos, *Automation* **2025**, *6*, 21.

[14] K. Darvish, M. Skreta, Y. Zhao, N. Yoshikawa, S. Som, M. Bogdanovic, Y. Cao, H. Hao, H. Xu, A. Aspuru-Guzik, A. Garg, F. Shkurti, *Matter* **2025**, *8*, 101897.

[15] B. P. MacLeod, F. G. L. Parlane, T. D. Morrissey, F. Häse, L. M. Roch, K. E. Dettelbach, R. Moreira, L. P. E. Yunker, M. B. Rooney, J. R. Deeth, V. Lai, G. J. Ng, H. Situ, R. H. Zhang, M. S. Elliott, T. H. Haley, D. J. Dvorak, A. Aspuru-Guzik, J. E. Hein, C. P. Berlinguette, *Sci. Adv.* **2020**, *6*, eaaz8867.

[16] D. Salley, G. Keenan, J. Grizou, A. Sharma, S. Martín, L. Cronin, *Nat. Commun.* **2020**, *11*, 2771.

[17] E. E. A. W. Councill, N. B. Axtell, T. Truong, Y. Liang, A. L. Aposhian, K. G. I. Webber, Y. Zhu, Y. Cong, R. H. Carson, R. T. Kelly, *SLAS Technol.* **2021**, *26*, 311.

[18] A. Kopyl, Y. Yew, J. W. Ong, T. Hiscox, C. Young, M. Muradoglu, T. W. Ng, *J. Chem. Educ.* **2024**, *101*, 640.

[19] P. A. Ferreira, F. M. De Oliveira, E. I. De Melo, A. E. De Carvalho, B. G. Lucca, V. S. Ferreira, R. A. B. Da Silva, *Anal. Chim. Acta* **2021**, *1169*, 338568.

[20] A. L. Silva, G. M. D. S. Salvador, S. V. F. Castro, N. M. F. Carvalho, R. A. A. Munoz, *Front. Chem.* **2021**, *9*, 684256.

[21] I. Oh, M. A. Pence, N. G. Lukhanin, O. Rodríguez, C. M. Schroeder, J. Rodríguez-López, *Device* **2023**, *1*, 100103.

[22] G. D. O'Neil, S. Ahmed, K. Halloran, J. N. Janusz, A. Rodríguez, I. M. Terrero Rodríguez, *Electrochem. Commun.* **2019**, *99*, 56.
[23] Z. Huang, A. Mu, L. Wu, B. Yang, Y. Qian, J. Wang, *ACS Sustain. Chem. Eng.* **2022**, *10*, 7786.
[24] L. F. Arenas, C. Ponce De León, F. C. Walsh, *Curr. Opin. Electrochem.* **2019**, *16*, 117.
[25] Y. Liang, H. Job, R. Feng, F. Parks, A. Hollas, X. Zhang, M. Bowden, J. Noh, V. Murugesan, W. Wang, *Cell Rep. Phys. Sci.* **2023**, *4*, 101633.
[26] P. T. Kissinger, W. R. Heineman, *J. Chem. Educ.* **1983**, *60*, 702.
[27] N. Elgrishi, K. J. Rountree, B. D. McCarthy, E. S. Rountree, T. T. Eisenhart, J. L. Dempsey, *J. Chem. Educ.* **2018**, *95*, 197.
[28] M. H. Chakrabarti, R. A. W. Dryfe, E. P. L. Roberts, *Electrochimica Acta* **2007**, *52*, 2189.
[29] H. Gursu, M. Gencten, Y. Sahin, *Int. J. Electrochem. Sci.* **2018**, *13*, 875.
[30] H. Gürsu, M. Gençten, Y. Şahin, *Ionics* **2018**, *24*, 3641.
[31] E. P. Randviir, *Electrochimica Acta* **2018**, *286*, 179.
[32] C. Sandford, M. A. Edwards, K. J. Klunder, D. P. Hickey, M. Li, K. Barman, M. S. Sigman, H. S. White, S. D. Minteer, *Chem. Sci.* **2019**, *10*, 6404.
[33] R. S. Nicholson, *Anal. Chem.* **1965**, *37*, 1351.
[34] I. Lavagnini, R. Antiochia, F. Magno, *Electroanalysis* **2004**, *16*, 505.
[35] J. Newman, W. Tiedemann, *J. Electrochem. Soc.* **1993**, *140*, 1961.
[36] A. Hashibon, *Solid State Ion.* **2002**, *149*, 167.
[37] F. Zhang, J. Liu, I. Ivanov, M. C. Hatzell, W. Yang, Y. Ahn, B. E. Logan, *Biotechnol. Bioeng.* **2014**, *111*, 1931.
[38] M. A. Pence, G. Hazen, J. Rodríguez-López, *Curr. Opin. Electrochem.* **2025**, *51*, 101679.
[39] C. Chen, G. Dai, Y. Gao, P. Xu, W. He, S. Feng, X. Zhu, Y. Zhao, *Energy Mater.* **2024**, *4*.
[40] M. Shin, C. Noh, Y. Chung, Y. Kwon, *Chem. Eng. J.* **2020**, *398*, 125631.
[41] A. M. Abdel-Aziz, H. H. Hassan, I. H. A. Badr, *ACS Omega* **2022**, *7*, 34127.

Appendix

G-code for positioning three-electrode holder

```
G21 ; set units to millimeters
G90 ; use absolute coordinates
G1 X20 Y140 Z150 ; corner coordinates
G4 P1000 ; wait for 1 sec for removing
; measurement 1
G1 X22 Y136 Z38 ; coordinates of well 1
G1 X22 Y136 Z28 ; Z-9 duck into well 1
G4 P5000 ; wait for 5 sec for measurement 1
G1 X22 Y136 Z50 ; leave well 1
G1 X22 Y136 Z150 ; moving up
G1 X20 Y140 Z150 ; corner coordinates with higher Z for removing pencil graphite
G4 P10000 ; wait for 10 sec for removing
;cleansing 1
G1 X22 Y127 Z38 ; Y-9 moving to cleaning well 1
G1 X22 Y127 Z28 ; cleaning(1)
G1 X22 Y127 Z38 ;
G1 X22 Y127 Z28 ; cleaning(2)
G1 X22 Y127 Z38 ;
G1 X22 Y127 Z28 ; cleaning(3)
G1 X22 Y127 Z38 ;
G1 X22 Y127 Z28 ; cleaning(4)
G1 X22 Y127 Z38 ;
G1 X22 Y127 Z28 ; cleaning(5)
G1 X22 Y127 Z38 ;
G1 X22 Y127 Z28 ; cleaning(6)
G1 X22 Y127 Z38 ;
G1 X20 Y140 Z150 ; corner coordinates with higher Z for new pencil graphite
G4 P5000 ; wait for 5 sec for changing new pencil graphite
; measurement 2
G1 X31 Y136 Z38 ; coordinates of well 2
G1 X31 Y136 Z28 ; Z-9 duck into well 2
G4 P5000 ; wait for 5 sec for measurement 2
G1 X31 Y136 Z38 ; leave well 2
G1 X31 Y136 Z150 ; moving up
G1 X20 Y140 Z150 ; corner coordinates with higher Z for removing pencil graphite
G4 P10000 ; wait for 10 sec for removing
;cleansing 2
G1 X31 Y127 Z38 ; Y-9 moving to cleaning well 2
G1 X31 Y127 Z28 ; cleaning(1)
G1 X31 Y127 Z38;
G1 X31 Y127 Z28 ; cleaning(2)
```

```
G1 X31 Y127 Z38 ;
G1 X31 Y127 Z28 ; cleaning(3)
G1 X31 Y127 Z38 ;
G1 X31 Y127 Z28 ; cleaning(4)
G1 X31 Y127 Z38 ;
G1 X31 Y127 Z28 ; cleaning(5)
G1 X31 Y127 Z38 ;
G1 X31 Y127 Z28 ; cleaning(6)
G1 X31 Y127 Z38 ;
G1 X20 Y140 Z150; corner coordinates with higher Z for new pencil graphite
G4 P5000 ; wait for 5 sec for changing new pencil graphite
; measurement 3
G1 X40 Y136 Z38 ; coordinates of well 3
G1 X40 Y136 Z28 ; Z-9 duck into well 3
G4 P5000 ; wait for 5 sec for measurement 3
G1 X40 Y136 Z50 ; leave well 3
G1 X40 Y136 Z150 ; moving up
G1 X20 Y140 Z150 ; corner coordinates with higher Z for removing pencil graphite
G4 P10000 ; wait for 10 sec for removing
;cleansing 3
G1 X40 Y127 Z38 ; Y-9 moving to cleaning well 3
G1 X40 Y127 Z28 ; cleaning(1)
G1 X40 Y127 Z38;
G1 X40 Y127 Z28 ; cleaning(2)
G1 X40 Y127 Z38 ;
G1 X40 Y127 Z28 ; cleaning(3)
G1 X40 Y127 Z38 ;
G1 X40 Y127 Z28 ; cleaning(4)
G1 X40 Y127 Z38 ;
G1 X40 Y127 Z28 ; cleaning(5)
G1 X40 Y127 Z38 ;
G1 X40 Y127 Z28 ; cleaning(6)
G1 X40 Y127 Z38 ;
G1 X20 Y140 Z150; corner coordinates with higher Z for new pencil graphite
G4 P5000 ; wait for 5 sec for changing new pencil graphite
; measurement 4
G1 X49 Y136 Z38 ; coordinates of well 4
G1 X49 Y136 Z28 ; Z-9 duck into well 4
G4 P5000 ; wait for 5 sec for measurement 4
G1 X49 Y136 Z50 ; leave well 4
G1 X49 Y136 Z150 ; moving up
G1 X20 Y140 Z150 ; corner coordinates with higher Z for removing pencil graphite
G4 P10000 ; wait for 10 sec for removing
;cleansing 4
```

```
G1 X49 Y127 Z38 ; Y-9 moving to cleaning well 4
G1 X49 Y127 Z28 ; cleaning(1)
G1 X49 Y127 Z38;
G1 X49 Y127 Z28 ; cleaning(2)
G1 X49 Y127 Z38 ;
G1 X49 Y127 Z28 ; cleaning(3)
G1 X49 Y127 Z38 ;
G1 X49 Y127 Z28 ; cleaning(4)
G1 X49 Y127 Z38 ;
G1 X49 Y127 Z28 ; cleaning(5)
G1 X49 Y127 Z38 ;
G1 X49 Y127 Z28 ; cleaning(6)
G1 X49 Y127 Z38 ;
G1 X20 Y140 Z150; corner coordinates with higher Z for new pencil graphite
G4 P5000 ; wait for 5 sec for changing new pencil graphite
; measurement 5
G1 X58 Y136 Z38 ; coordinates of well 5
G1 X58 Y136 Z28 ; Z-9 duck into well 5
G4 P5000 ; wait for 5 sec for measurement 5
G1 X58 Y136 Z50 ; leave well 5
G1 X58 Y136 Z150 ; moving up
G1 X20 Y140 Z150 ; corner coordinates with higher Z for removing pencil graphite
G4 P10000 ; wait for 10 sec for removing
;cleansing 5
G1 X58 Y127 Z38 ; Y-9 moving to cleaning well 5
G1 X58 Y127 Z28 ; cleaning(1)
G1 X58 Y127 Z38;
G1 X58 Y127 Z28 ; cleaning(2)
G1 X58 Y127 Z38 ;
G1 X58 Y127 Z28 ; cleaning(3)
G1 X58 Y127 Z38 ;
G1 X58 Y127 Z28 ; cleaning(4)
G1 X58 Y127 Z38 ;
G1 X58 Y127 Z27 ; cleaning(5)
G1 X58 Y127 Z38 ;
G1 X58 Y127 Z28 ; cleaning(6)
G1 X58 Y127 Z38 ;
G1 X20 Y140 Z150; corner coordinates with higher Z for new pencil graphite
G4 P5000 ; wait for 5 sec for changing new pencil graphite
; measurement 6
G1 X67 Y136 Z38 ; coordinates of well 6
G1 X67 Y136 Z28 ; Z-9 duck into well 6
G4 P5000 ; wait for 5 sec for measurement 6
G1 X67 Y136 Z50 ; leave well 6
```

```
G1 X67 Y136 Z150 ; moving up
G1 X20 Y140 Z150 ; corner coordinates with higher Z for removing pencil graphite
G4 P10000 ; wait for 10 sec for removing
;cleansing 6
G1 X67 Y127 Z38 ; Y-9 moving to cleaning well 6
G1 X67 Y127 Z28 ; cleaning(1)
G1 X67 Y127 Z38;
G1 X67 Y127 Z28 ; cleaning(2)
G1 X67 Y127 Z38 ;
G1 X67 Y127 Z28 ; cleaning(3)
G1 X67 Y127 Z38 ;
G1 X67 Y127 Z28 ; cleaning(4)
G1 X67 Y127 Z38 ;
G1 X67 Y127 Z28 ; cleaning(5)
G1 X67 Y127 Z38 ;
G1 X67 Y127 Z28 ; cleaning(6)
G1 X67 Y127 Z38 ;
G1 X20 Y140 Z150; corner coordinates with higher Z for new pencil graphite
G4 P5000 ; wait for 5 sec for changing new pencil graphite
; measurement 7
G1 X76 Y136 Z38 ; coordinates of well 7
G1 X76 Y136 Z28 ; Z-9 duck into well 7
G4 P5000 ; wait for 5 sec for measurement 7
G1 X76 Y136 Z50 ; leave well 7
G1 X76 Y136 Z150 ; moving up
G1 X20 Y140 Z150 ; corner coordinates with higher Z for removing pencil graphite
G4 P10000 ; wait for 10 sec for removing
;cleansing 7
G1 X76 Y127 Z38 ; Y-9 moving to cleaning well 7
G1 X76 Y127 Z28 ; cleaning(1)
G1 X76 Y127 Z38;
G1 X76 Y127 Z28 ; cleaning(2)
G1 X76 Y127 Z38 ;
G1 X76 Y127 Z28 ; cleaning(3)
G1 X76 Y127 Z38 ;
G1 X76 Y127 Z28 ; cleaning(4)
G1 X76 Y127 Z38 ;
G1 X76 Y127 Z28 ; cleaning(5)
G1 X76 Y127 Z38 ;
G1 X76 Y127 Z28 ; cleaning(6)
G1 X76 Y127 Z38 ;
G1 X20 Y140 Z150; corner coordinates with higher Z for new pencil graphite
G4 P5000 ; wait for 5 sec for changing new pencil graphite
; measurement 8
```

```
G1 X85 Y136 Z38 ; coordinates of well 8
G1 X85 Y136 Z28 ; Z-9 duck into well 8
G4 P5000 ; wait for 5 sec for measurement 8
G1 X85 Y136 Z50 ; leave well 8
G1 X85 Y136 Z150 ; moving up
G1 X20 Y140 Z150 ; corner coordinates with higher Z for removing pencil graphite
G4 P10000 ; wait for 10 sec for removing
;cleansing 8
G1 X85 Y127 Z38 ; Y-9 moving to cleaning well 8
G1 X85 Y127 Z28 ; cleaning(1)
G1 X85 Y127 Z38;
G1 X85 Y127 Z28 ; cleaning(2)
G1 X85 Y127 Z38 ;
G1 X85 Y127 Z28 ; cleaning(3)
G1 X85 Y127 Z38 ;
G1 X85 Y127 Z28 ; cleaning(4)
G1 X85 Y127 Z38 ;
G1 X85 Y127 Z28 ; cleaning(5)
G1 X85 Y127 Z38 ;
G1 X85 Y127 Z28 ; cleaning(6)
G1 X85 Y127 Z38 ;
G1 X20 Y140 Z150; corner coordinates with higher Z for new pencil graphite
G4 P5000 ; wait for 5 sec for changing new pencil graphite
; measurement 9
G1 X94 Y136 Z38 ; coordinates of well 9
G1 X94 Y136 Z28 ; Z-9 duck into well 9
G4 P5000 ; wait for 5 sec for measurement 9
G1 X94 Y136 Z50 ; leave well 9
G1 X94 Y136 Z150 ; moving up
G1 X20 Y140 Z150 ; corner coordinates with higher Z for removing pencil graphite
G4 P10000 ; wait for 10 sec for removing
;cleansing 9
G1 X94 Y127 Z38 ; Y-9 moving to cleaning well 9
G1 X94 Y127 Z28 ; cleaning(1)
G1 X94 Y127 Z38;
G1 X94 Y127 Z28 ; cleaning(2)
G1 X94 Y127 Z38 ;
G1 X94 Y127 Z28 ; cleaning(3)
G1 X94 Y127 Z38 ;
G1 X94 Y127 Z28 ; cleaning(4)
G1 X94 Y127 Z38 ;
G1 X94 Y127 Z28 ; cleaning(5)
G1 X94 Y127 Z38 ;
G1 X94 Y127 Z28 ; cleaning(6)
```

```
G1 X94 Y127 Z38 ;
G1 X20 Y140 Z150; corner coordinates with higher Z for new pencil graphite
G4 P5000 ; wait for 5 sec for changing new pencil graphite
; measurement 10
G1 X103 Y136 Z38 ; coordinates of well 10
G1 X103 Y136 Z28 ; Z-9 duck into well 10
G4 P5000 ; wait for 5 sec for measurement 10
G1 X103 Y136 Z50 ; leave well 10
G1 X103 Y136 Z150 ; moving up
G1 X20 Y140 Z150 ; corner coordinates with higher Z for removing pencil graphite
G4 P10000 ; wait for 10 sec for removing
;cleansing 10
G1 X103 Y127 Z38 ; Y-9 moving to cleaning well 10
G1 X103 Y127 Z28 ; cleaning(1)
G1 X103 Y127 Z38;
G1 X103 Y127 Z28 ; cleaning(2)
G1 X103 Y127 Z38 ;
G1 X103 Y127 Z28 ; cleaning(3)
G1 X103 Y127 Z38 ;
G1 X103 Y127 Z28 ; cleaning(4)
G1 X103 Y127 Z38 ;
G1 X103 Y127 Z28 ; cleaning(5)
G1 X103 Y127 Z38 ;
G1 X103 Y127 Z28 ; cleaning(6)
G1 X103 Y127 Z38 ;
G1 X20 Y140 Z150; corner coordinates with higher Z for new pencil graphite
G4 P5000 ; wait for 5 sec for changing new pencil graphite
; measurement 11
G1 X112 Y136 Z38 ; coordinates of well 11
G1 X112 Y136 Z28 ; Z-9 duck into well 11
G4 P5000 ; wait for 5 sec for measurement 11
G1 X112 Y136 Z50 ; leave well 11
G1 X112 Y136 Z150 ; moving up
G1 X20 Y140 Z150 ; corner coordinates with higher Z for removing pencil graphite
G4 P10000 ; wait for 10 sec for removing
;cleansing 11
G1 X112 Y127 Z38 ; Y-9 moving to cleaning well 11
G1 X112 Y127 Z28 ; cleaning(1)
G1 X112 Y127 Z38;
G1 X112 Y127 Z28 ; cleaning(2)
G1 X112 Y127 Z38 ;
G1 X112 Y127 Z28 ; cleaning(3)
G1 X112 Y127 Z38 ;
G1 X112 Y127 Z28 ; cleaning(4)
```

```
G1 X112 Y127 Z38 ;
G1 X112 Y127 Z28 ; cleaning(5)
G1 X112 Y127 Z38 ;
G1 X112 Y127 Z28 ; cleaning(6)
G1 X112 Y127 Z38 ;
G1 X20 Y140 Z150; corner coordinates with higher Z for new pencil graphite
G4 P5000 ; wait for 5 sec for changing new pencil graphite
; measurement 12
G1 X121 Y136 Z38 ; coordinates of well 12
G1 X121 Y136 Z28 ; Z-9 duck into well 12
G4 P5000 ; wait for 5 sec for measurement 12
G1 X121 Y136 Z50 ; leave well 12
G1 X121 Y136 Z150 ; moving up
G1 X20 Y140 Z150 ; corner coordinates with higher Z for removing pencil graphite
G4 P10000 ; wait for 10 sec for removing
;cleansing 12
G1 X121 Y127 Z38 ; Y-9 moving to cleaning well 12
G1 X121 Y127 Z28 ; cleaning(1)
G1 X121 Y127 Z38;
G1 X121 Y127 Z28 ; cleaning(2)
G1 X121 Y127 Z38 ;
G1 X121 Y127 Z28 ; cleaning(3)
G1 X121 Y127 Z38 ;
G1 X121 Y127 Z28 ; cleaning(4)
G1 X121 Y127 Z38 ;
G1 X121 Y127 Z28 ; cleaning(5)
G1 X121 Y127 Z38 ;
G1 X121 Y127 Z28 ; cleaning(6)
G1 X121 Y127 Z38 ;
G1 X20 Y140 Z150; corner coordinates with higher Z for new pencil graphite
G4 P5000 ; wait for 5 sec for changing new pencil graphite
```